Transportation Research Part B 150 (2021) 101–120

Contents lists available at ScienceDirect

Transportation Research Part B

journal homepage: www.elsevier.com/locate/trb

Perimeter control with real-time location-varying cordon

Ye Li [a], Reza Mohajerpoor [b], Mohsen Ramezani [a,*]

[a] The University of Sydney, School of Civil Engineering, Sydney, Australia
[b] Data61, CSIRO, Sydney, Australia

ARTICLE INFO

Keywords:
Network fundamental diagram
Gating
Time-varying cordon
Optimal control
Congestion management

ABSTRACT

With unbalanced travel demand distribution over time and space, a stationary cordon location hinders the full potential of perimeter flow control based on network Macroscopic Fundamental Diagram (MFD). This paper introduces a perimeter control method wherein the region boundaries alter in real-time to tackle propagation of local pockets of congestion. The nonlinear dynamics of the heterogeneous traffic network are modelled as a switching system. The linearization of the derived switching nonlinear dynamics is conducted considering the accumulation heterogeneity. A Linear Quadratic Regulator (LQR) is employed for gating the flow exchange between regions to minimize network congestion. Several scenarios are examined comparing perimeter control schemes with static and dynamic cordons. Results pinpoint the proposed LQR control with location-varying cordon strategy and a moderate switching interval significantly reduces the vehicles total time spent in the network.

1. Introduction

To improve traffic efficiency in urban networks, numerous traffic signal control policies have been developed in the past few decades. Majority of these signal control policies are nominally designed for isolated intersections (e.g. Lee et al., 2017; Mohajerpoor et al., 2019; Mohajerpoor and Cai, 2020), or small-scale coordinated traffic signals (e.g. He et al., 2014; Wada et al., 2018; Li et al., 2018; Ma et al., 2018). These control strategies often require detailed local traffic information and encompass hefty computational costs. Introduction of network macroscopic fundamental diagram (MFD) enabled a promising direction towards the network-level systematic congestion management at a very low computational cost through perimeter flow control (Geroliminis et al., 2012; Ramezani et al., 2015; Yang et al., 2018; Lei et al., 2019; Ingole et al., 2020; Li et al., 2021), congestion pricing (Daganzo and Lehe, 2015; Simoni et al., 2015; Amirgholy and Gao, 2017; Gu et al., 2018; Zheng and Geroliminis, 2020), route guidance Yildirimoglu et al. (2015), departure time management (Yildirimoglu and Ramezani, 2020), and ride-sourcing operation control (Ramezani and Nourinejad, 2018) among others.

MFD describes a well-defined, low-scatter, and nonlinear relationship between mean weighted flow and vehicle accumulation of a network. It was first introduced by Godfrey (1969), and was empirically demonstrated in Geroliminis and Daganzo (2008) utilizing field data of Yokohama, Japan. The literature shows a heterogeneous network does not exhibit a well-defined MFD due to the occurrence of the hysteresis (e.g. Gayah and Daganzo, 2011). Partitioning a heterogeneous network into several homogeneous subregions is a solution to cope with the MFD hysteresis (e.g. Saeedmanesh and Geroliminis, 2017; Saedi et al., 2020). The partitioning further enables introduction of perimeter flow control as an effective traffic control method.

Perimeter flow control monitors and regulates vehicle densities in multiple regions aiming at maximizing the trip completion rate in the entire traffic network (e.g. Haddad and Zheng, 2018; Zhong et al., 2018; Keyvan-Ekbatani et al., 2019; Haddad and Mirkin,

* Corresponding author.
E-mail address: mohsen.ramezani@sydney.edu.au (M. Ramezani).

https://doi.org/10.1016/j.trb.2021.05.016
Received 17 November 2020; Received in revised form 20 February 2021; Accepted 30 May 2021
0191-2615/© 2021 Elsevier Ltd. All rights reserved.

2020). It has been introduced for two-region (e.g. Geroliminis et al., 2012; Haddad, 2017; Ding et al., 2017) and multi-region networks (e.g. Csikós et al., 2017; Yang et al., 2018; Mohajerpoor et al., 2020; Sirmatel et al., 2021). Theoretical and empirical advancements on MFD modelling and estimation (e.g. Saffari et al., 2020; Aghamohammadi and Laval, 2020; Mariotte et al., 2020a; Paipuri et al., 2020), have enabled the application of numerous perimeter control techniques, such as feedback control (Keyvan-Ekbatani et al., 2015; Ampountolas et al., 2017; Keyvan-Ekbatani et al., 2021), model predictive control (MPC) (Geroliminis et al., 2012; Yildirimoglu et al., 2018; Han et al., 2020; Sirmatel and Geroliminis, 2021), adaptive control (Haddad and Zheng, 2018; Haddad and Mirkin, 2020), and robust control (Haddad, 2015; Mohajerpoor et al., 2020).

To date, all of the existing perimeter flow control schemes consider *static* (or fixed) region boundaries (e.g. Kouvelas et al., 2017; Haddad and Zheng, 2018; Zhong et al., 2018; Haddad and Mirkin, 2020; Guo and Ban, 2020; Ren et al., 2020; Ding et al., 2020; Su et al., 2020). This strict limitation prevents the MFD-based network control paradigms to agilely respond to the time-varying nature of congestion propagation, especially in networks with time- and spatially-varying travel demands. Due to the intrinsic complexities of network traffic dynamics and the spatial and temporal demand fluctuations, splitting the congested and uncongested regions needs to be revisited recurrently in real-time. In light of that, we propose a novel traffic responsive cordon switching algorithm integrated within a *location-varying* perimeter control method.

A large number of perimeter control schemes have only considered networks with well-defined MFDs (e.g. Ingole et al., 2020; Yang et al., 2019; Fu et al., 2020), ignoring the hysteresis phenomenon. Another shortcoming of the majority of the existing perimeter control methods is disregarding the possible heavy concentration of vehicles at region boundaries in result of cordon metering, which may lead to uneven distribution of vehicle accumulation and local pockets of congestion. Recently, Haddad (2017), Ni and Cassidy (2019) addresses the impacts of queued vehicles by segregating vehicles into travelling and queuing. The proposed location-varying perimeter control method can (indirectly) address both limitations.

A perimeter control with location-varying cordon enables tackling temporal and spatial local pockets of congestion. For instance, Fig. 1 shows a schematic of a network that is split into 19 smaller homogeneous subregions (shown as hexagons), and two regions that separate the congested (Region 2) and less-congested (Region 1) areas. The borderline separating the two regions is highlighted using solid green and dashed red lines, representing the perimeter controllers that manipulate transfer flows between the regions. The figure delineates a possible scenario that the cordon switches at two different time steps. First, uncongested Subregion 17 is deallocated from Region 2 (Fig. 1(b)); and next Subregion 8 is allocated to Region 2 due to getting more congested (Fig. 1(c)). The cordon initially has border with all subregions except Subregion 19 (see Fig. 1(a)), and cordon switching enables direct control of Subregion 19 as shown in Fig. 1(b, c). Our proposed cordon selection algorithm recurrently identifies and ranks the most congested subregions based on a proposed measure called 'protection index', and clusters them into the protected region in a smooth process. Note that allocating subregions to different regions alters the regional MFD and thus a switching system emerges. Design and modelling the switched system are among the methodological contributions of this paper.

The traffic flow dynamics are modelled at two (consistent) levels of aggregation, subregion- and region-level. The subregions are assumed to be homogeneously congested each with a well-defined MFD. That is, an average speed describes the trip progression of vehicles inside the subregions. A number of subregions embodies a region. Thus regions are heterogeneously congested and accordingly scattered regional MFDs are observed. The region-level model takes the spatial density heterogeneity into consideration, hence hysteresis emerges in the modelled MFDs at the region level. Further, because of the change in the cordon and the shape of regions over time, vehicles can cross the region boundaries *multiple* times. A simple en-route route choice model is integrated in the subregion-level model, which considers the current fastest paths (i.e. a succession of subregions) from the origin subregion to the destination one. This necessitates to devise a regional route choice procedure. The route choice model in region-level MFD model comprises two variables which estimate the regional route ratios (see pink arrows in Fig. 1(a) showing regional routes 1–1 and 1–2–1) and the ratio of transfer flows between regions based on the destinations of the vehicles (see yellow arrows in Fig. 1(a) showing the ratio of transfer flow between Region 1 and Region 2 with the final destination in Region 2 and Region 1).

The main contributions of this paper are threefold: (i) developing a perimeter control method with location-varying cordon to capture the congestion evolution in the network by separating congested and uncongested subregions into two regions; (ii) introducing a more realistic model by permitting vehicles to cross the region boundaries multiple times; and (iii) designing a Linear Quadratic Regulator (LQR) controller to obtain the optimal transfer flow rates between regions for a *switching system*. To synthesize the controller, the region-level nonlinear dynamics are linearized at optimal set-points derived from the desired characteristics of the network considering the density heterogeneity impacts. A Linear Quadratic Regulator (LQR) controller is designed every time the cordon switches to optimally regulate the gated flow between the regions. The proposed dynamic perimeter control algorithm is examined on a congested and heterogeneous traffic network comprising 19 homogeneous subregions. That is, the regional model is used to design the controller while the subregion-level model is the only model as the traffic simulator. The results pinpoint the indispensable advantages that the proposed location-varying cordon paradigm brings to empower the perimeter controller, in a way that over 23% reduction in the total time spent (TTS) is achieved due to applying the dynamic cordon strategy when implementing the LQR controller.

The rest of the paper is organized as follows. Section 2 presents the dynamic models in both subregion and region levels; Section 3 introduces the network control strategies; the numerical experiments are presented in Section 4, and the paper is summarized together with sketching future research directions in Section 5.

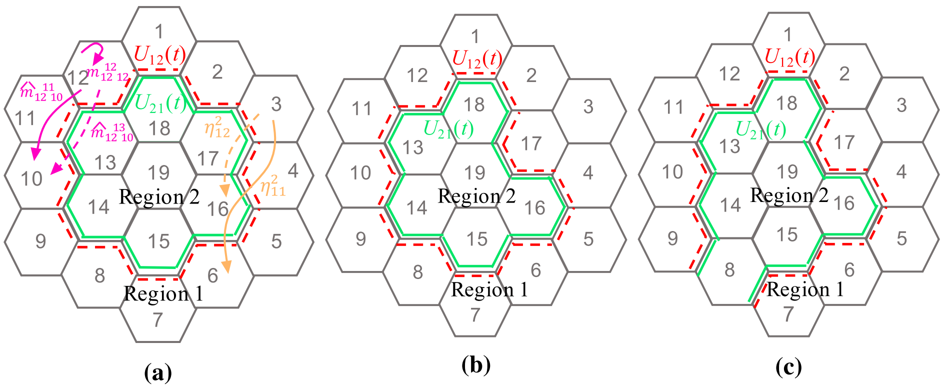

Fig. 1. A large-scale two-region heterogeneous network comprising 19 homogeneous subregions. The borderline separating the two regions is highlighted using a solid green and a dashed red line, representing gating flow exchange from Region 2 to 1 and from Region 1 to 2, respectively. (a) The initial boundary of the two regions, Region 1 encompasses Subregions 1 to 12, and Region 2 is formed by Subregions 13 to 19, where Subregion 19 is not directly influenced by the perimeter control traffic signals. (b) First cordon switching when Subregion 17 becomes uncongested and is allocated to Region 1. (c) Second cordon switching where Subregion 8 becomes congested and is allocated to Region 2. Note that the proposed controller can possibly shrink Region 2 to only include one subregion, e.g., Subregion 19. Details of modelling are given in Section 2.

2. Network traffic flow modelling

In this section, we develop two traffic flow models based on MFD to explain the subregional (see Section 2.1) and regional level (see Section 2.2) dynamics of traffic propagation in the network. We assume the urban network is partitioned into a set of homogeneous subregions, $\mathscr{R}$, that form a heterogeneous traffic network comprising two regions. The subregion level MFD model describes detailed traffic dynamics of each subregion, integrates a current-best route choice model, and considers the effect of the boundary and receiving capacities. The region level MFD model incorporates variant trip lengths in each region, considers heterogeneity of spatial congestion distribution, and embeds a simple route choice model because vehicles can pass region boundaries multiple times. In addition, the regional MFD model is used for controller synthesize, while the subregion level model is applied as traffic simulator. Note that the region and subregion level models are consistent and interconnected (see Section 2.3). In the sequel, the corresponding variables and parameters for the region and subregion level models are denoted by upper-case and lower-case letters, respectively. The nomenclature is listed in Appendix A.

2.1. Subregion-level traffic flow model

The subregion-level model tracks the evolution of accumulation of vehicles in each subregion over time based on MFD dynamics. Each subregion demonstrates a well-defined MFD that relates the average speed of the vehicles to the total number of vehicles inside the subregion. Let $n_{ij}(t)$ [veh], $i, j \in \mathscr{R}$, denote the number of vehicles in Subregion i with destination in Subregion j; and $n_i(t) = \sum_{j=1}^{|\mathscr{R}|} n_{ij}(t)$ [veh] denote the accumulation of Subregion i at time t. Therefore, the accumulation in Region I is $N_I(t) = \sum_{i\in\mathscr{R}_I(t)} n_i(t)$, where $\mathscr{R}_I(t)$ is the set of subregions in Region I at time t. Note that $\mathscr{R}_I(t)$ alters every time instance that the cordon changes as presented in Section 3.1.

The internal outflow of Subregion i at time t is denoted by $m^i_{ii}(t)$ [veh/s]. The external outflow of Subregion i with final destination in Subregion j through the immediate Subregion h is denoted by $m^h_{ij}(t)$ [veh/s],[1] $h \in \phi_i$, where ϕ_i is the set of subregions directly reachable from Subregion i. The average trip length of vehicles in Subregion i that travel within the subregion and vehicles that travel to Subregion $h \in \phi_i$ are denoted by $l_{ii}(t)$ and $l_{ih}(t)$ [m], respectively. Therefore, assuming slow-varying traffic conditions, Subregion i internal and external outflows read

$$m^i_{ii}(t) = \frac{n_{ii}(t)}{n_i(t)} \cdot \frac{p_i(n_i(t))}{l_{ii}(t)}, \tag{1a}$$

$$m^h_{ij}(t) = \theta^h_{ij}(t) \cdot \frac{n_{ij}(t)}{n_i(t)} \cdot \frac{p_i(n_i(t))}{l_{ih}(t)} \quad i \neq j, h \in \phi_i, \tag{1b}$$

where $p_i(n_i(t)) = d_{3i} n_i(t)^3 + d_{2i} n_i(t)^2 + d_{1i} n_i(t)$ with $\{d_{3i}, d_{2i}, d_{1i}\} \in \mathbb{R}$ is the production MFD of homogeneous Subregion i; and $\theta^h_{ij}(t) \in [0, 1]$ shows the time-varying proportion of vehicles in Subregion i with destination in Subregion j that the next immediate subregion in their path is Subregion h. Accordingly, we have $\sum_{h\in\phi_i} \theta^h_{ij}(t) = 1$. The subregion-level model integrates a route choice model that assumes vehicles make en-route decisions based on the instantaneous speed of each subregion. That is, k-shortest macro

[1] We assume the vehicles making internal trips in a subregion do not leave the subregion, i.e. $m^h_{ii}(t) = 0$ ($i \neq h$ and $i, h \in \mathscr{R}$). The assumption is reasonable if subregions pertain compact and convex shapes, so that staying in a subregion for every vehicle complies with the shortest path constraint.

paths (i.e. a series of subregions) are considered (through Dijkstra's algorithm) at every time instant between each subregion pair based on the instantaneous travel time of subregions and macro paths. A simple logit model is then employed to assign path flows to the k-shortest macro paths according to their travel times. This results in obtaining $\theta_{ij}^{h}(t)$. Note that this routing model is different than the equilibrium concept and may be categorized as an *en-route current-best* routing strategy.

The perimeter flow control output is denoted as, $u_{ih}(t)$, that regulates the proportion of external outflow that is allowed to transfer from Subregion i to Subregion $h \in \phi_i$ at time t. This pertains to the cordon on which the perimeter flow control is activated (i.e. the boundary between the regions). In other words, $u_{ih}(t)$ is equal to its maximum practical value between any two subregions that does not constitute the regions boundary. Note that the outgoing transfer flow, $m_{ij}^{h}(t) \cdot u_{ih}(t)$, may not be realized if the neighbour Subregion h is congested and there are not enough space available for incoming flows. Therefore, the receiving capacity of subregions is incorporated into the model. The realized external outflow from Subregion i with destination in Subregion j through Subregion h, $\hat{m}_{ij}^{h}(t)$ [veh/s], is estimated from the minimum of the outgoing transfer flow, boundary capacity between Subregions i and h (b_{ih} [veh/s]), as well as a part of receiving capacity of Subregion h ($r_h(n_h(t))$ proportional to the incoming transfer flows from all subregions around Subregion h:

$$\hat{m}_{ij}^{h}(t) = \min\left(m_{ij}^{h}(t)u_{ih}(t), b_{ih}, \frac{m_{ij}^{h}(t)u_{ih}(t)}{\sum_{s_1\in\phi_h}\sum_{s_2\in\mathcal{R},s_2\neq s_1} m_{s_1 s_2}^{h}(t)u_{s_1 h}(t)} \cdot r_h(n_h(t)) \right). \tag{2}$$

The receiving capacity of Subregion h, $r_h(n_h(t))$ [veh/s], is defined as,

$$r_h(n_h(t)) = r_h^{\max} \cdot (1 - \frac{n_h(t)}{n_h^{\text{jam}}}), \tag{3}$$

where $r_h^{\max}$ is the maximum receiving capacity of Subregion h, and $n_h(t)$ and n_h^{jam} [veh] are the number of vehicles in Subregion h at time t and the jam accumulation of Subregion h, respectively. Note that the receiving capacity proposed in Ramezani et al. (2015) considered each incoming flow to Subregion h independently. On the other hand, Eq. (2) takes into account all the incoming flows collectively and distribute the available receiving capacity of Subregion h proportionally (demand pro-rata as investigated in Mariotte et al. (2020b)). The estimation of the maximum receiving capacity, $r_h^{\max}$, and the exact form of receiving capacity of subregions require further investigations and validation with field data. This is a challenge for future research as obtaining data at a congestion level close to jam accumulation is rare to occur. See Mariotte et al. (2020b) for further study of variants of the receiving capacity models.

Let $q_{ij}(t)$ [veh/s] represent the exogenous travel demand generated in Subregion i with destination in Subregion j. The mass conservation equations of the subregion-level model tracking the accumulations of vehicles with respect to their destinations are ($i, j \in \mathcal{R}$):

$$\frac{\mathrm{d}n_{ii}(t)}{\mathrm{d}t} = q_{ii}(t) - m_{ii}^{i}(t) + \sum_{h\in\phi_i} \hat{m}_{hi}^{i}(t), \tag{4a}$$

$$\frac{\mathrm{d}n_{ij}(t)}{\mathrm{d}t} = q_{ij}(t) - \sum_{h\in\phi_i} \hat{m}_{ij}^{h}(t) + \sum_{h\in\phi_i} \hat{m}_{hj}^{i}(t), \quad i \neq j. \tag{4b}$$

Note that we take into account the effects of perimeter control in modelling the receiving capacity, i.e. Eq. (2), therefore the subregional conservation equations do not include the related perimeter control variables.

2.2. Region-level traffic flow model

The region-level model tracks the accumulation of vehicles in each region dynamically over time based on MFD dynamics. The MFD of each region reflects the aggregation of the production MFDs of all subregions inside the region. Through this aggregation, region MFD might exhibit hysteresis. To model the hysteresis, the heterogeneity of links densities inside the region should be considered.

Let $N_I(t)$ [veh] and $|\mathcal{R}_I(t)|$ denote the number of vehicles in Region I and the number of subregions in Region I at time t. In the most homogeneous condition, the accumulation of each subregion would be $N_I(t)/|\mathcal{R}_I(t)|$. To incorporate the impacts of density heterogeneity on MFD, the standard deviation (STD) of density of all links in Region I, $\sigma(N_I(t))$, is considered. The production MFD of Region I, $P_I(N_I(t), \sigma(N_I(t)))$, can be expressed by the product of a cubic polynomial and an exponential function (Ramezani et al., 2015):

$$P_I(N_I(t), \sigma(N_I(t))) = \left(\tilde{D}_{3I} N_I(t)^3 + \tilde{D}_{2I} N_I(t)^2 + \tilde{D}_{1I} N_I(t)\right) \left(D_{\sigma_I} \cdot e^{\beta_I \left(\sigma(N_I(t)) - \sigma_I^{\text{het}}\right)} + (1 - D_{\sigma_I}) \right), \tag{5}$$

where $\tilde{D}_{3I}, \tilde{D}_{2I}, \tilde{D}_{1I}, D_{\sigma_I}$, and β_I are constant scalar parameters that are estimated using empirical data. Moreover, σ_I^{het} is the standard deviation of density of all links in Region I with minimum heterogeneity where the link density distribution in each subregion inside Region I follows the negative binomial distribution. That is, σ_I^{het} [veh] is the standard deviation of the aggregation of $|\mathcal{R}_I(t)|$ negative binomial distributions each with mean density of $N_I(t)/|\mathcal{R}_I(t)|$. The cubic polynomial on the right-hand-side of Eq. (5) is the upper-envelope production MFD of Region I, while the second term reflects the effect of density heterogeneity of Region I. With minimal heterogeneity, $\sigma(N_I(t))$ tends to σ_I^{het} and thus there is no decrease in the production of the region. However, an increase in $\sigma(N_I(t))$ results in drop in the production. The details of deriving Eq. (5) can be found in (Ramezani et al., 2015).

The second modelling consideration is the route choice at the regional scale. The border separating the two regions can form non-compact and non-convex regions shapes, which triggers the necessity of taking into account the vehicles that cross the region boundary multiple times to follow their en-route shortest path (see Fig. 1). The proposed region-level model incorporates this by introducing two time-varying variables, see Eq. (6) below. Further, Eq. (9) and (10) capture the route choice behaviour using the real-time information feedback from the subregion-level dynamic model.

Let $N_{IJ}(t)$ [veh] ($I, J \in \{1, 2\}$) denote the vehicle accumulation in Region I with destination in Region J at time t. Moreover, $N_I(t) = N_{II}(t) + N_{IJ}(t)$ [veh] indicates the total number of vehicles in Region I at time t. The total trip completion of Region I at time t comprises three components; (i) $M^I_{II}(t)$ [veh/s] is the internal trip completion rate in Region I at time t, (ii) $M^J_{II}(t)$ [veh/s] is the external outflow from Region I with origin and destination in Region I that traverse through Region J at time t, and (iii) $M^J_{IJ}(t)$ [veh/s] is the external outflow from Region I to Region J as their destination at time t. These outflow components can be modelled as:

$$M^I_{II}(t) = \Theta^I_{II}(t) \cdot \frac{N_{II}(t)}{N_I(t)} \cdot \frac{P_I(N_I(t), \sigma(N_I(t)))}{L_{II}(t)}, \tag{6a}$$

$$M^J_{II}(t) = \eta^J_{II}(t) \cdot \Theta^J_{II}(t) \cdot \frac{N_{II}(t)}{N_I(t)} \cdot \frac{P_I(N_I(t), \sigma(N_I(t)))}{L_{IJ}(t)}, \tag{6b}$$

$$M^J_{IJ}(t) = \eta^J_{IJ}(t) \cdot \Theta^J_{IJ}(t) \cdot \frac{N_{IJ}(t)}{N_I(t)} \cdot \frac{P_I(N_I(t), \sigma(N_I(t)))}{L_{IJ}(t)}, \tag{6c}$$

where $L_{II}(t)$ and $L_{IJ}(t)$ are respectively the average trip lengths of vehicles with origins in Region I and have destinations in Region I and Region J; and $\Theta^I_{II}(t)$ and $\Theta^J_{II}(t) \in [0, 1]$ ($I \neq J$ and $\Theta^I_{II}(t) + \Theta^J_{II}(t) = 1$) demonstrate the time-varying proportions of the number of vehicles with origin and destination in Region I that remain in the region and cross the region's boundary, respectively. It is intuitive that $\Theta^J_{IJ}(t) = 1$ since all vehicles with origin in Region I and destination in Region J have to cross the region's perimeter.

Furthermore, the region-level model takes into account the ratio of outflows at the region boundary over the subregions transfer flows inside the region. Accordingly, variables $0 \le \eta^J_{II}(t), \eta^J_{IJ}(t) \le 1$ are defined such that $\eta^J_{II}(t)$ represents the ratio of the transfer flows with the final destination in Region I that pass region boundaries a time t. Similarly, $\eta^J_{IJ}(t)$ shows the ratio of the transfer flows with the final destination in Region J that cross the boundary between Region I and J at time t. The introduction of these ratios is a byproduct of the way regional average trip lengths are estimated in Eq. (8) such that immediate outflows from the subregions sharing the boundary is considered.

To manipulate the transfer flows between regions, the regions periphery are gated by a set of coordinated traffic signals that enforce the perimeter control actions $0 \le U^{\min} \le U_{IJ}(t), U_{JI}(t) \le U^{\max} \le 1$, ($I \neq J$). The perimeter control is acting on the region boundaries, such that there are no additional restrictions on vehicles travelling through subregion boundaries inside a region. In other words, the inter-transfer flows between any two subregions are not controlled, i.e. $u_{ij}(t) = U^{\max}$. The perimeter controller is active on the subregion boundaries that are part of the region boundaries, i.e. $u_{ij}(t) = U_{IJ}(t)$ ($i \in \mathscr{R}_I, j \in \mathscr{R}_J$). Accordingly, once the border of subregions i and j on the cordon moves inside a region due to the cordon change, it becomes uncontrolled. Note that vehicles that transfer from Region I to Region J are either added to the vehicles with destinations in Region J (with the rate of $U_{IJ} \cdot M^J_{IJ}$), or added to the vehicles with destinations in Region I (with the rate of $U_{IJ} \cdot M^J_{II}$). In addition, the receiving capacity is not considered for the region-level model, since the perimeter controller is expected to prevent hypercongestion in the regions.

Let $Q_{IJ}(t)$ [veh/s] ($I, J \in \{1, 2\}$) denote the exogenous travel demand from Region I to Region J at time t. Consequently, the mass conservation equations for the region-level MFD dynamics read as ($I, J = \{1, 2\}$):

$$\frac{\mathrm{d}N_{II}(t)}{\mathrm{d}t} = Q_{II}(t) - M^I_{II}(t) - U_{IJ}(t) \cdot M^J_{II}(t) + U_{JI}(t) \cdot M^I_{JI}(t), \tag{7a}$$

$$\frac{\mathrm{d}N_{IJ}(t)}{\mathrm{d}t} = Q_{IJ}(t) - U_{IJ}(t) \cdot M^J_{IJ}(t) + U_{JI}(t) \cdot M^I_{JJ}(t). \tag{7b}$$

The variables $L(t) = \{L_{II}(t), L_{IJ}(t)\}$, $\Theta(t) = \{\Theta^I_{II}(t), \Theta^J_{II}(t)\}$, and $\Xi(t) = \{\eta^J_{II}(t), \eta^J_{IJ}(t)\}$ are formally defined in the forthcoming section using real-time information feedback from the subregion-level measurements.

2.3. Relationship between subregion-level measurements and region-level variables

The region-level and subregion-level dynamics are correlated and consistent. Majority of variables in Eq. (6) and Eq. (7) are estimated from the subregion-level model measurements. The number of vehicles in Region I at time t, $N_I(t) = N_{II}(t) + N_{IJ}(t)$, can be estimated based on the measurements of subregions as, $N_{II}(t) = \Sigma_{i,j \in \mathscr{R}_I(t)} n_{ij}(t)$ and $N_{IJ}(t) = \Sigma_{i \in \mathscr{R}_I(t)} \Sigma_{j \in \mathscr{R}_J(t)} n_{ij}(t)$. Similarly the exogenous travel demands can be estimated as, $Q_{II}(t) = \Sigma_{i,j \in \mathscr{R}_I(t)} q_{ij}(t)$ and $Q_{IJ}(t) = \Sigma_{i \in \mathscr{R}_I(t)} \Sigma_{j \in \mathscr{R}_J(t)} q_{ij}(t)$. In addition, the subregion-level perimeter control, $u_{ij}(t)$, are equal to the region-level perimeter control, $U_{IJ}(t)$ ($i \in \mathscr{R}_I(t), j \in \mathscr{R}_J(t)$). The perimeter control synthesis based on LQR theory is explained in Section 3. Note that a second level controller to break down regional $U(t)$ to subregional $u(t)$ (see for example Ramezani et al. (2015)), can be investigated as a future research to complement the dynamic cordon feature.

The average trip length in Region I for vehicles with destinations respectively in Region I and in Region J, i.e. $L_{II}(t)$ and $L_{IJ}(t)$, are estimated based on the subregion-level measurements as

$$L_{II}(t) = \frac{\sum_{i,j \in \mathscr{R}_I(t)} n_{ij}(t)}{\sum_{i \in \mathscr{R}_I(t)} n_i(t)} \cdot \frac{\sum_{i \in \mathscr{R}_I(t)} p_i(n_i(t))}{\sum_{i \in \mathscr{R}_I(t)} m^i_{ii}(t)}, \tag{8a}$$

$$L_{IJ}(t) = \frac{\sum_{i\in\mathcal{R}_I(t)}\sum_{j\in\mathcal{R}}\sum_{h\in(\mathcal{R}_J(t)\cap\phi_i)}\theta_{ij}^h(t)\cdot n_{ij}(t)}{\sum_{i\in\mathcal{R}_I(t)} n_i(t)} \cdot \frac{\sum_{i\in\mathcal{R}_I(t)} p_i(n_i(t))}{\sum_{i\in\mathcal{R}_I(t)}\sum_{j\in\mathcal{R}}\sum_{h\in(\mathcal{R}_J(t)\cap\phi_i)}\hat{m}_{ij}^h(t)} \quad i \neq j. \tag{8b}$$

The above equations hold alike logic in terms of regional model, i.e. $L_{II}(t) \sim N_{II}(t)\ /\ N_I(t)\cdot P_I(N_I(t))\ /\ M_{II}(t)$ and $L_{IJ}(t) \sim N_{IJ}(t)\ /\ N_I(t)\cdot P_I(N_I(t))\ /\ M_{IJ}(t)$. Note that in Eq. (8b) all the outflows from Region I towards Region J is considered irrespective of the final destinations of the transfer flows.

The regional route choice ratios of vehicles from Region I with destinations in Region I that respectively travel through Regions I and J, $\Theta_{II}^I(t)$ and $\Theta_{II}^J(t)$, are estimated using the subregion-level measurements as

$$\Theta_{II}^I(t) = \frac{\sum_{i\in\mathcal{R}_I(t)} m_{ii}^i(t) + \sum_{i\in\mathcal{R}_I(t)}\sum_{j\in\mathcal{R}_I(t)}\sum_{h\in(\mathcal{R}_I(t)\cap\phi_i)}\hat{m}_{ij}^h(t)}{\sum_{i\in\mathcal{R}_I(t)} m_{ii}^i(t) + \sum_{i\in\mathcal{R}_I(t)}\sum_{j\in\mathcal{R}_I(t)}\sum_{h\in(\mathcal{R}_I(t)\cap\phi_i)}\hat{m}_{ij}^h(t) + \sum_{i\in\mathcal{R}_I(t)}\sum_{j\in\mathcal{R}_I(t)}\sum_{h\in(\mathcal{R}_J(t)\cap\phi_i)}\hat{m}_{ij}^h(t)}, \tag{9a}$$

$$\Theta_{II}^J(t) = \frac{\sum_{i\in\mathcal{R}_I(t)}\sum_{j\in\mathcal{R}_I(t)}\sum_{h\in(\mathcal{R}_J(t)\cap\phi_i)}\hat{m}_{ij}^h(t)}{\sum_{i\in\mathcal{R}_I(t)} m_{ii}^i(t) + \sum_{i\in\mathcal{R}_I(t)}\sum_{j\in\mathcal{R}_I(t)}\sum_{h\in(\mathcal{R}_I(t)\cap\phi_i)}\hat{m}_{ij}^h(t) + \sum_{i\in\mathcal{R}_I(t)}\sum_{j\in\mathcal{R}_I(t)}\sum_{h\in(\mathcal{R}_J(t)\cap\phi_i)}\hat{m}_{ij}^h(t)}. \tag{9b}$$

Fig. 1(a) provides a visual aid for the transfer flows in calculating $\Theta(t)$ and $\Xi(t)$ variables, as indicated by different colour arrows. The numerators of Eq. (9a) and (9b) indicate the amount of outflows corresponding to the internal flows that remain in Region I and the transfer flows that cross the region boundary, respectively. The denominators (which are the same) are the sum of the internal and transfer flows with origins in Region I and destinations in Region I.

Furthermore, the time-dependent variables $\eta_{II}^J(t)$ and $\eta_{IJ}^J(t)$ are estimated using subregion measurements as:

$$\eta_{II}^J(t) = \frac{\sum_{i\in\mathcal{R}_I(t)}\sum_{j\in\mathcal{R}_I(t)}\sum_{h\in(\mathcal{R}_J(t)\cap\phi_i)}\hat{m}_{ij}^h(t)}{\sum_{i\in\mathcal{R}_I(t)}\sum_{j\in\mathcal{R}_I(t)}\sum_{h\in(\mathcal{R}_I(t)\cap\phi_i)}\hat{m}_{ij}^h(t) + \sum_{i\in\mathcal{R}_I(t)}\sum_{j\in\mathcal{R}_I(t)}\sum_{h\in(\mathcal{R}_J(t)\cap\phi_i)}\hat{m}_{ij}^h(t)}, \tag{10a}$$

$$\eta_{IJ}^J(t) = \frac{\sum_{i\in\mathcal{R}_I(t)}\sum_{j\in\mathcal{R}_J(t)}\sum_{h\in(\mathcal{R}_J(t)\cap\phi_i)}\hat{m}_{ij}^h(t)}{\sum_{i\in\mathcal{R}_I(t)}\sum_{j\in\mathcal{R}_J(t)}\sum_{h\in(\mathcal{R}_I(t)\cap\phi_i)}\hat{m}_{ij}^h(t) + \sum_{i\in\mathcal{R}_I(t)}\sum_{j\in\mathcal{R}_J(t)}\sum_{h\in(\mathcal{R}_J(t)\cap\phi_i)}\hat{m}_{ij}^h(t)}. \tag{10b}$$

The numerator of Eq. (10a) represents the sum of the transfer flows of vehicles with origins and destinations in Region I while their next immediate subregions along their paths belong to Region J. The denominator of Eq. (10a) is the sum of flows of vehicles with origins and destinations in Region I irrespective of their immediate subregion. Thus, $\eta_{II}^J(t)$ denotes the ratio of vehicles from I to I that cross the region boundary at time t while other vehicles from I to I might cross the boundary at a later time. This distinction is crucial since a large number of vehicles would first travel in subregions of Region I prior to crossing the boundary. Those vehicles should not be counted in estimation of $M_{II}^J(t)$.

Similarly, the numerator of Eq. (10b) expresses the sum of the transfer flows of vehicles with origins in Region I and destinations in Region J while their next immediate subregions along their paths belong to Region J. The denominator of Eq. (10b) represents the sum of flows of vehicles with origins in Region I and destinations in Region J irrespective of their immediate subregion. Thus, $\eta_{IJ}^J(t)$ denotes the ratio of vehicles from I to J that cross the region boundary at time t while other vehicles from I to J might cross the boundary at a later time. For instance, vehicles in Subregion 3 with destination in Subregion 19 in Fig. 1(c) should not be counted in $M_{12}^2(t_1)$ estimation at time $t_1 > 0$ in Eq. (6c).

3. Controller design

The proposed perimeter controller with location-varying cordon consists of two components: (i) a cordon location changing algorithm introduced in Section 3.1 and (ii) a model-based perimeter transfer flow regulator presented in Section 3.2. The cordon switching algorithm determines the cordon on which the traffic signals that belong to the perimeter controller are located. This is devised such that subregions are dynamically grouped together over time partitioning the network into two regions ensuring Region 2 consists of congested subregions that require protection against the inflows from Region 1 (see Fig. 1). The accumulation of subregions are used to define the subregion *protection index* that triggers the switching of the cordon following a criterion elaborated in Section 3.1.

An LQR scheme is considered to balance the accumulation of each region through gating the transfer flows between the regions. The aim of the controller is to maintain the accumulation of each region at a desirable level. LQR control design is based on the linearization of the nonlinear model in Eq. (7), which is discussed in Section 3.2.2. Recurrently clustering the most congested subregions into the protected region, results into a switching model. Thus, model linearization and controller design problems should be reiterated every time the cordon switches. Fortunately, both problems can be solved instantly in less than a few seconds that promotes the control algorithm as a practical candidate for this application. The closed-loop control system architecture is depicted in Fig. 2.

3.1. Cordon switching algorithm

We design the algorithm such that the boundary of the protected region can alter after a predefined time steps, called switching interval $\kappa > 0$. This is to prevent abrupt changes in regions' boundaries and to make the proposed switching scheme smooth and practical. Moreover to this end, at most one subregion (among the borderline subregions) can be reassigned to the other region each time switching occurs.

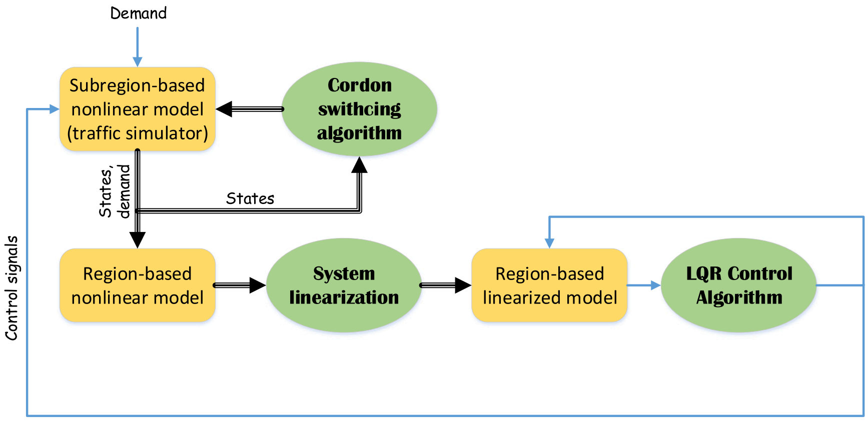

Fig. 2. The closed-loop architecture of the proposed dynamic cordon perimeter control method based on LQR. The thick black arrows indicate the triggered operations at the switching time-steps, κ. The blue arrows indicate the continuous flow of information. Note that the subregion-level model is employed as the traffic simulator to examine the controller performance. The region-level model is adopted to design the controller. (For interpretation of the colours in this figure, the reader is referred to the web version of the manuscript).

The proposed cordon switching algorithm works based on the *density weight* of each Subregion i and the *outflow pressure* of its surrounding subregions, $h \in \phi_i$. We define the Subregion i density weight as

$$w_i(t) = \left(\frac{n_i(t)}{n_i^{\mathrm{cr}}}\right)^2, \tag{11}$$

where n_i^{cr} [veh] is the time-invariant critical accumulation of Subregion i. The density weight provides a normalized criterion for evaluating the congestion level of every subregion, such that further enables the simplicity in computing subregion protection indexes, in which case $w_i(t) \leq 1$ indicates Subregion i is uncongested, and otherwise it is congested. Note that the density weight is in the quadratic form to put more emphasis on hypercongested subregions when calculating the protection index of the subregions. Also note that using mean speed of Subregion i (i.e. $v_i(t)$) to calculate $w_i(t)$ is a valid alternative, while there is no significant difference between the two options as both indicate the congestion level of the subregion.

The outflow pressure of Subregion h at time t, $s_h(t)$, is defined as,

$$s_h(t) = \frac{p_h(n_h(t))}{p_h^{\max} \cdot (|\phi_h| + 1)} \qquad \forall h \in \phi_i, \tag{12}$$

where $|\phi_h|$ denotes the size of set ϕ_h (subregions that are neighbour of Subregion h) and $p_h^{\max}$ is the maximum value of the production MFD of Subregion h. The outflow pressure of Subregion h reflects the normalized and expected outflow from the subregion towards its neighbours. That is, higher outflow pressure means more inflow towards the neighbouring subregions and hence the chance of them becoming more congested is higher. Note that the outflow pressure of Subregion h at time t, $s_h(t)$, is a function of production MFD of Subregion h, i.e. it has an increasing relationship with the accumulation of Subregion h, $n_h(t)$, up to the critical accumulation of Subregion h and a decreasing trend once the accumulation exceeds the critical value. Furthermore, the $(|\phi_h| + 1)$ term in the denominator of Eq. (12) accounts for the number of neighbouring subregions plus the Subregion h itself to consider the effect of internal outflow.

Thereafter, the *protection index* of Subregion i at time t, $\lambda_i(t)$, is defined as

$$\lambda_i(t) = w_i(t) \cdot \sum_{h \in \phi_i} s_h(t) \qquad \forall i \in \mathscr{R}, \tag{13}$$

which reflects the level of protection required for Subregion i to be sustained from the overcongestion by the perimeter controller. The higher the protection index, it is more desirable to allocate the subregion in the protected Region 2.

The regional protection index interprets the average protection index of the subregions in that region which is defined as,

$$\bar{\Lambda}_I(t) = \frac{\Sigma_{i \in \mathscr{R}_I(t)} \lambda_i(t)}{|\mathscr{R}_I(t)|}. \tag{14}$$

Considering the above definition, the cordon switching algorithm at each switching time seeks the borderline among all admissible cordons that results in the highest difference between the regional protection indexes of the two regions considering the constraint that at most only one subregion can be relocated to the other region. In other words, the new borderline corresponds with the maximum regional protection index difference when reallocating a single subregion from current Region I, i.e. $\mathscr{R}_I(t)$, to Region J that builds the new Region I, $\mathscr{R}_I^*(t)$ and the new Region J, $\mathscr{R}_J^*(t)$. If the current borderline still maximizes the protection index difference between the two regions at the switching time-step, the algorithm is repeated in the next time-steps until a switching occurs, and then there will be no switching for the next κ steps. The pseudo-code of the cordon switching algorithm is provided in Algorithm 1.

Algorithm 1: Pseudo-code of the cordon switching algorithm.

```
allocations = [subregions IDs, regions IDs]
%first column is from 1 to the total number of subregions |R|, second column is corresponding regional IDs I or J
if κ time steps have passed since the last cordon change then
  D_init(t) = |Λ̄_I(t) − Λ̄_J(t)|, using Eq. (11) - Eq. (14)
  %Calculate the absolute value of the average protection index difference between the two regions
  for i = 1 : |R| do
    Change allocation of Subregion i to the other region to form two new regions, R*_I(t) and R*_J(t)
    Check connectivity
    %to ensure there are at most two new regions in total
    if Check connectivity is true then
      D^i_new(t) = |Λ̄_{I*}(t) − Λ̄_{J*}(t)|, using Eq. (11) - Eq. (14)
      %Calculate the absolute value of average protection index difference between the two temporally new formed regions,
      i.e. R*_I(t) and R*_J(t)
    end if
  end for
end if
Find max_i D^i_new(t)
if max_i D^i_new(t) > D_init(t) then
  R_I(t) = R*_I(t) and R_J(t) = R*_J(t)
  update allocations
end if
```

The switching rate κ is a crucial hyper-parameter that needs to be carefully adjusted to maximize the performance of the controller. It is shown in the case studies (see Section 4) that fast switching similar to slow switching (i.e. small/large switching intervals) may deteriorate the performance of the control system. According to the theories on the stability of switched linear systems (see e.g. Zhang and Shi, 2009; Lin and Antsaklis, 2009) there is a minimum switching interval that guarantees the stability of the system. This minimum interval is the desired dwelling period for the switching paradigm when applying a linear control strategy, including the LQR scheme as explained in the next section.

3.2. LQR control framework

LQR controller is one of the semantic and most powerful linear control methods. To apply the LQR theory to obtain the perimeter control outputs, the nonlinear region-level model should be linearized. To linearize the region-level dynamic model in Eq. (7), the Steady-State (SS) traffic condition should be specified by obtaining the nominal (or SS) states, control inputs, and demands. Given the location-varying nature of the cordon, the SS traffic conditions switch from time to time whenever the location of the cordon gets updated. Let the cordon change at instants $t_{\rho_s} \in \{t_1, t_2, \dots\}$, $0 < t_1 < t_2 < \cdots$. The predefined desired accumulation of Region $I = \{1,2\}$ at time $t \geq t_{\rho_s}$ can be expressed as $N^{\mathrm{d}}_{s,\rho_s}$, $s \in \Omega_n = \{11,12,21,22\}$. The nominal regional accumulations, demand, and control outputs are denoted by N^*_{s,ρ_s}, Q^*_{s,ρ_s}, and U^*_{r,ρ_s}, $r \in \Omega_u = \{12,21\}$, respectively.

3.2.1. The steady-state traffic condition

The first step to linearize the nonlinear region-level model is to obtain the SS of the model. Defining $P^*_{I,\rho_s} = P_I(N^*_{I,\rho_s}, \sigma(N^*_{I,\rho_s}))$, from Eqs. (6) and (7) the equilibrium dynamics of the model can be derived as:

$$Q^*_{II,\rho_s} - \Theta^{I*}_{II,\rho_s}\frac{N^*_{II,\rho_s}P^*_{I,\rho_s}}{N^*_{I,\rho_s}L^*_{II,\rho_s}} - U^*_{IJ,\rho_s}\Theta^{J*}_{II,\rho_s}\eta^{J*}_{II,\rho_s}\frac{N^*_{II,\rho_s}P^*_{I,\rho_s}}{N^*_{I,\rho_s}L^*_{IJ,\rho_s}} + U^*_{JI,\rho_s}\Theta^{I*}_{JI,\rho_s}\eta^{I*}_{JI,\rho_s}\frac{N^*_{JI,\rho_s}P^*_{J,\rho_s}}{N^*_{J,\rho_s}L^*_{JI,\rho_s}} = 0, \tag{15a}$$

$$Q^*_{IJ,\rho_s} - U^*_{IJ,\rho_s}\Theta^{J*}_{IJ,\rho_s}\eta^{J*}_{IJ,\rho_s}\frac{N^*_{IJ,\rho_s}P^*_{I,\rho_s}}{N^*_{I,\rho_s}L^*_{IJ,\rho_s}} + U^*_{JI,\rho_s}\Theta^{I*}_{JJ,\rho_s}\eta^{I*}_{JJ,\rho_s}\frac{N^*_{JJ,\rho_s}P^*_{J,\rho_s}}{N^*_{J,\rho_s}L^*_{JI,\rho_s}} = 0, \tag{15b}$$

where Q^*_{II,ρ_s}, Q^*_{IJ,ρ_s}, Θ^{I*}_{II,ρ_s}, Θ^{J*}_{II,ρ_s}, Θ^{J*}_{IJ,ρ_s}, η^{J*}_{II,ρ_s}, η^{J*}_{IJ,ρ_s}, L^*_{II,ρ_s}, and L^*_{JI,ρ_s} are the SS parameters estimated from empirical data.[2] The steady-state control outputs should lie within the range $[U^{*\min}, U^{*\max}]$, where $U^{\min} \leq U^{*\min} < U^{*\max} \leq U^{\max}$ are predetermined

[2] A practical way is to employ the estimated trip length $L(t_{\rho_s})$, as well as $\Theta(t_{\rho_s})$ and $\Xi(t_{\rho_s})$ parameters at the cordon switching instances t_{ρ_s} as their SS values. This approach is effective due to the slow variations of dynamic parameters in a large-scale traffic network. Moreover, the maximum expected demand of the new regions can be assigned as the SS demand to ensure the controller is designed for the highest expected inflow to each region.

scalars. Accordingly, as demonstrated in Mohajerpoor et al. (2020) the SS traffic conditions can be obtained from the following optimization program:

$$\begin{aligned}\min_{N^*_{I,\rho_s},N^*_{II,\rho_s},U^*_{IJ,\rho_s}} \; & \sum_{I=1}^{2} \beta_I (N^*_{I,\rho_s} - N^{\mathrm{d}}_{I,\rho_s})^2 \\ & \text{Subject to :} \\ & \text{Eq. (15)}, \\ & 0 \le \{N^*_{I,\rho_s}, N^*_{II,\rho_s}\} \le \alpha_I N^{\mathrm{jam}}_{I,\rho_s}, \\ & U^{*\min} \le U^*_{IJ,\rho_s} \le U^{*\max},\end{aligned} \tag{O1}$$

where $N^{\mathrm{jam}}_{I,\rho_s}$ is the jam accumulation of Region I; $0 < \alpha_I < 1$ is a constant coefficient to specify the maximum allowable SS accumulation of Region $I \in \{1,2\}$; and β_I is a positive weighting coefficient that characterizes the relative importance of Region I with respect to the other region. The desired accumulations $N^{\mathrm{d}}_{I,\rho_s}$ can be chosen to be smaller and close to the critical accumulations $N^{\mathrm{cr}}_{I,\rho_s}$ to maximize the outflow of each region. Note that the number of subregions in Region I might change every time the regions boundary is updated. Thus, the jam, desired, and SS accumulation of each region change accordingly.

Note that problem (O1) is a nonlinear program that should be solved for a local optima every time the regions boundaries are updated, whence the dynamic parameters of each region including the desired and jam accumulations alter. Due to the nonlinear nature of equality constraints (15), simultaneous fulfilment of the equality and inequality constrains of (O1) can be intractable. In such occasion, one might increase the tolerance on the equality constrains to a sufficiently higher level and maintain the inequality constraints. This amendment helps in finding local optimal accumulations and control signals in the majority of traffic conditions, while equations (15) can be slightly violated that is acceptable due to uncertainties in the estimated steady-state parameters.

3.2.2. Linearized dynamic equations

Now, the model Eq. (7) can be linearized at every instance that the cordon changes which results in a new SS traffic condition. Note that as the signal timings of the intersections at the perimeter control cordon change every cycle time, and to facilitate the practicality of the proposed perimeter control method, the control output, U_{IJ}, should be discrete. Accordingly, we discretize the continuous-time linearized (region-level) dynamics of the network using the sample-and-hold technique with sample size of $\tau > 0$, where τ is the common fixed cycle time of the cordon's signalized intersections. This step-size empowers the controller to alter the signal timings only at the end of each cycle, and results in the following difference equation:

$$\Delta N_{\rho_s}[k+1] = A_{\rho_s}\Delta N_{\rho_s}[k] + B_{\rho_s}\Delta U_{\rho_s}[k] + D_{\rho_s}\Delta Q_{\rho_s}[k] + \mathbf{O}\left(\Delta L_{\rho_s}[k], \Delta\Theta_{\rho_s}[k], \Delta\eta_{\rho_s}[k]\right), \tag{16}$$

where $\Delta N_{\rho_s}[k] = \left[\Delta N_{s,\rho_s}[k]\right] \in \mathbb{R}^{\boldsymbol{s_n}}$ is the state vector; $\Delta U_{\rho_s}[k] = \left[\Delta U_{r,\rho_s}[k]\right] \in \mathbb{R}^{\boldsymbol{s_u}}$ is the control output; $\Delta Q_{\rho_s}[k] = \left[\Delta Q_{s,\rho_s}[k]\right] \in \mathbb{R}^{\boldsymbol{s_n}}$ is the demand disturbance. These variables are the infinitesimal variations from the SS accumulations, control signals and demand, i.e., $\Delta N_{s,\rho_s}[k] = N_{s,\rho_s}[k] - N^*_{s,\rho_s}$, $\Delta U_{r,\rho_s}[k] = U_{r,\rho_s}[k] - U^*_{r,\rho_s}$, and $\Delta Q_{s,\rho_s}[k] = Q_{s,\rho_s}[k] - Q^*_{s,\rho_s}$ ($s \in \Omega_n$, $r \in \Omega_u$, $\boldsymbol{s_n} = 4$, and $\boldsymbol{s_u} = 2$). Furthermore, $\mathbf{O}\left(\Delta L_{\rho_s}[k], \Delta\Theta_{\rho_s}[k], \Delta\eta_{\rho_s}[k]\right) \in \mathbb{R}^{\boldsymbol{s_n}}$ is a negligible perturbation term due to the infinitesimal dynamics of parameters $L_{\rho_s} = [L_{IJ,\rho_s}] \in \mathbb{R}^4$, $\Theta_{\rho_s} = [\Theta^J_{II,\rho_s}] \in \mathbb{R}^4$, and $\eta_{\rho_s} = [\eta^K_{IJ,\rho_s}] \in \mathbb{R}^4$ ($I, J, K \in \{1,2\}$) about their SS values. Matrices $A_{\rho_s} \in \mathbb{R}^{\boldsymbol{s_n}\times\boldsymbol{s_n}}$, $B_{\rho_s} \in \mathbb{R}^{\boldsymbol{s_n}\times\boldsymbol{s_u}}$, and $D_{\rho_s} \in \mathbb{R}^{\boldsymbol{s_n}\times\boldsymbol{s_n}}$ are obtained from the linearization procedure, and are demonstrated in Appendix B. Note that these matrices are constant when the cordon is fixed, and they change once the region's perimeter is changed (reflected by the ρ_s subscript). It is assumed that all states are measured in real-time.

A challenge in deriving the linearized matrices A_{ρ_s} and B_{ρ_s} is dealing with the time-varying STD of the network's density $\sigma(N_{I,\rho_s}(t))$, $I = \{1,2\}$. Indeed, there is no closed-form one-to-one mapping between the accumulation STD of a region and its average density. The accumulation STD of each region is in addition influenced by the current density heterogeneity and the distribution of travel demand across the region, and it can be *measured* or estimated in real-time via the measured density of the subregions within the region. However, to calculate the elements of A_{ρ_s} and B_{ρ_s}, the derivative of $\sigma(N_{I,\rho_s}(t))$ with respect to $N_{I,\rho_s}(t)$ is required at the equilibrium SS traffic condition (see Appendix B). A solution to overcome this issue is proposed in Appendix C.

3.2.3. Controller synthesis

Based on the linearized dynamic model, the perimeter control output is defined as $U[k] = \mathrm{sat}\left(U^*_{\rho_s} + \Delta U_{\rho_s}[k]\right)$, where $\mathrm{sat}(U[k]) = \left[\mathrm{sat}(U_{12}[k]), \mathrm{sat}(U_{21}[k])\right]^T$,

$$\mathrm{sat}(U_{IJ}[k]) \triangleq \begin{cases} U^{\max} & U_{IJ}[k] > U^{\max} \\ U_{IJ}[k] & U^{\min} \le U_{IJ}[k] \le U^{\max} \\ U^{\min} & U_{IJ}[k] < U^{\min}, \end{cases}$$

$\Delta U_{\rho_s}[k] = K_{\rho_s}\Delta N_{\rho_s}[k]$, and $K_{\rho_s} \in \mathbb{R}^{s_n\times s_n}$ is obtained via solving the following optimization problem:

$$\begin{aligned}
&\min_{K_{\rho_s}} \sum_{i=0}^{\infty} \Delta N^T_{\rho_s}[i] P_{\rho_s} \Delta N_{\rho_s}[i] + \Delta U^T_{\rho_s}[i] \Gamma_{\rho_s} \Delta U_{\rho_s}[i],\\
&\quad \text{Subject to :}\\
&\quad \text{Eq. (16)},\\
&\quad \Delta Q_{\rho_s} \equiv 0,\\
&\quad \mathbf{O}(\cdot,\cdot,\cdot) \equiv 0,
\end{aligned} \tag{O2}$$

wherein $P_{\rho_s} \in \mathbb{R}^{s_n\times s_n}$ and $\Gamma_{\rho_s} \in \mathbb{R}^{s_u\times s_u}$ are positive definite diagonal matrices predefined appropriately. The first term in the objective function drives the accumulation of each region towards its set point, and the second term is to ensure the boundedness of the control outputs. It is advised to set the elements of matrix P_{ρ_s} proportional to the reciprocal of the jam accumulation of the corresponding region to normalize the effects of accumulations, and set the elements of Γ_{ρ_s} small enough to result in reasonably bounded control outputs. Solution of (O2) can be sought from the solution ($\Pi_{\rho_s} \in \mathbb{S}^{s_n\times s_n}$) of the following discrete-time Riccati equation (Anderson and Moore, 2007):

$$A^T_{\rho_s}\Pi_{\rho_s}A_{\rho_s} - \Pi_{\rho_s} - (A^T_{\rho_s}\Pi_{\rho_s}B_{\rho_s})(B^T_{\rho_s}\Pi_{\rho_s}B_{\rho_s} + \Gamma_{\rho_s})^{-1}(B^T_{\rho_s}\Pi_{\rho_s}A_{\rho_s}) + P_{\rho_s} = 0, \tag{17}$$

and $K_{\rho_s} = \left(B^T_{\rho_s}\Pi_{\rho_s}B_{\rho_s} + \Gamma_{\rho_s}\right)^{-1} B^T_{\rho_s}\Pi_{\rho_s}A_{\rho_s}$.

In summary, the perimeter boundary changes following Algorithm 1 and the network maintains the updated boundary for at least κ time-steps. After every cordon switching, the control gain K_{ρ_s} is updated taking the sequel steps: (i) the steady state traffic condition is obtained from solving optimization problem (O1), (ii) the nonlinear region-based model of the network (7) is linearized at the steady-state traffic conditions and then discretized according to the difference equation (16), and eventually (iii) the control gain is obtained from solving Riccati equation (17). Note that other methods to derive the control gain can be developed as a future research work.

4. Numerical experiments

4.1. Settings

We study a simulation model of a complex heterogeneous traffic network that is divided into two regions that initially consist of 12 (in Region 1) and 7 (in Region 2) homogeneous subregions, as shown in Fig. 1(a). Without loss of generality, subregions pertain identical MFDs consistent with the one observed in Yokohama, Japan (see Geroliminis and Daganzo, 2008), i.e. $d_{3i} = 3.4216\times10^{-4}$, $d_{2i} = -6.8575$, and $d_{1i} = 3.4710\times10^4$, $\forall i \in \mathscr{R}$. Accordingly, the critical accumulation that maximizes the subregion production is $n_i^{\mathrm{cr}} = 3334$ [veh], and the jam accumulation is $n_i^{\mathrm{jam}} = 10000$ [veh]. The initial regional accumulations in Region 1 and Region 2 are assumed to be uncongested with $N_1(0) = 29008$ [veh] and $N_2(0) = 19297$ [veh].

It is assumed that all the gated intersections share a common cycle time of 60 s, thus the dynamic model, Eq. (7), is discretized with sample time of $\tau = 1$ [min]. Note that the traffic simulator, which is the subregion-level model (Eq. (4)), is implemented with a 0.01 [sec] discretization time-step, and the 1 [min] time-step is used for the controller synthesis as illustrated in Section 3.2.2. Moreover, to comply with operational constraints, the control outputs are lower and upper bounded by $U^{\min} = 0.1$ and $U^{\max} = 0.9$, respectively. A general peak-hour exogenous demand is applied, as shown in Fig. 3(a), with most of the demand generated from the subregions in Region 1 towards the subregions in Region 2 (subregions belong to Region 2 are assumed to be the downtown areas), and then the demands are gradually dropped to zero to ensure the network gets cleared at the end of simulation. Note that the regional demand values would alter with the shift of regions with dynamic cordon, whereas the OD demands in the subregion-level are identical across all control scenarios. Furthermore, the model embeds a stochastic en-route current-based route choice model to replicate a more realistic traffic simulation environment.

To investigate the effectiveness of the proposed controller, the Bang–Bang (BB) control strategy is chosen for comparison purposes. BB policy is a variable structure control method, wherein the control outputs take either minimum or maximum values at each time step. An effective policy proposed in Geroliminis et al. (2012) is chosen. In summary, if both regions are uncongested, i.e. $N_{I,\rho_s}[k] \le N^*_{I,\rho_s}$, we set $U_{IJ} = U^{\max}$; if only Region I is congested and Region J is uncongested, then $U_{IJ} = U^{\max}$ and $U_{JI} = U^{\min}$; and if both regions are congested and $N_{I,\rho_s}[k]/N^{\mathrm{jam}}_{I,\rho_s} > N_{J,\rho_s}[k]/N^{\mathrm{jam}}_{J,\rho_s}$, then $U_{IJ} = U^{\max}$ and $U_{JI} = U^{\min}$ ($I, J \in \{1,2\}$ and $I \ne J$). The proposed LQR algorithm contrary to the BB strategy can result in the full range of control outputs, rather than just the boundary values $U^{\min}$ and $U^{\max}$. However, the BB strategy is a robust nonlinear controller that can accommodate the abrupt changes in the regions' accumulations when the model does not comply with the linearized dynamic approximation. Moreover, the criterion for switching between the minimum and maximum boundary values can follow a more complex framework, such as the algorithm presented in Aalipour et al. (2018).

Four control scenarios are implemented on the simulation model to study the effectiveness of location-varying cordon integrated in the perimeter control: (a) Bang–Bang controller with static cordon, (b) LQR controller with static cordon, (c) Bang–Bang controller with dynamic cordon, and (d) LQR controller with dynamic cordon. Note that the OD demands in the subregion-level and other aspects of experiments are identical in all the studied control scenarios.

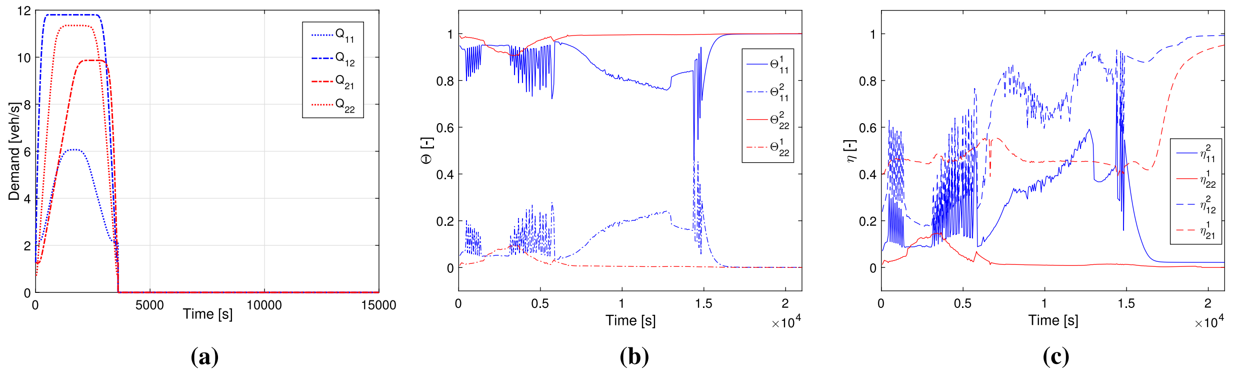

Fig. 3. (a) Regional demands in the network during the simulation period for the static cordon scenarios. The values of the (regional) demands would alter once the region boundaries change. However, the OD demands in the subregion-level are identical across all control scenarios. (b) $\Theta(t)$ and (c) $\Xi(t)$ parameters variations with time when applying the LQR + static cordon control algorithm.

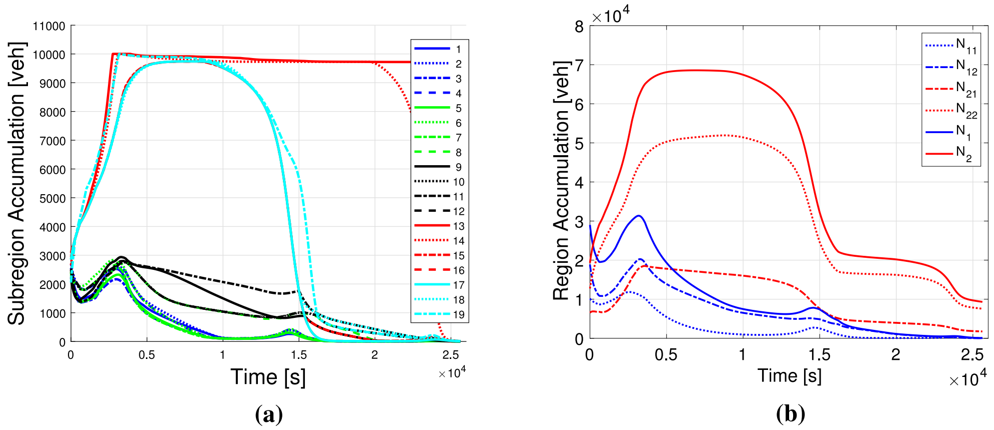

Fig. 4. Results of the no-control scenario ($U_{12}(t) = U_{21}(t) = 0.9$): (a) subregional and (b) regional accumulations for the whole simulation period. The accumulations of several subregions (i.e. Subregions 13–19) reach to (or very close to) the jam accumulation $n^{\text{jam}} = 10000$ and face gridlock during a long period, and accordingly Region 2 reaches to the hypercongested regime.

4.2. Results and discussion

Under the heterogeneous demand (Fig. 3(a)), the inner Subregions 13–19 become heavily congested if they are not protected using an effective perimeter control. This is highlighted by the simulation results from the 'no-control' scenario in Fig. 4, wherein maximum transfer flows between regions are enabled (i.e. $U_{12}(t) = U_{21}(t) = U^{\max} = 0.9$) with the static cordon sketched in Fig. 1(a). It can be observed that those subregions face gridlock in less than 1 hr, and the accumulations in Region 2 never cleared for the rest of the simulation.

Figs. 3(b) and 3(c) depict the time-varying nature of $\Theta(t)$ and $\Xi(t) = \{\eta^J_{II}(t), \eta^J_{IJ}(t)\}$ $(I, J \in \{1,2\}$ and $I \neq J)$, that shows the drivers, who choose the shortest path to their destinations, cross the regions' boundary multiple times. Given $\Theta^I_{II}(t) + \Theta^J_{II}(t) = 1$, Fig. 3(b) demonstrates $\Theta^I_{II}(t) > \Theta^J_{II}(t)$ that indicates the shortest paths chosen by travellers are tend to remain inside the region rather than cross the boundary multiple times. Moreover, $\Theta^2_{22}(t)$ is observed to be always greater than or equal to $\Theta^1_{11}(t)$, because the dynamic cordon stacks all the congested subregions in Region 2, which is the inner region with a compact shape. Therefore, there are less opportunities for vehicles to cross Region 1 if both origins and destinations are in Region 2. To add, Fig. 3(c) highlights that $\Xi(t)$ variables in the proposed model capture the time-varying ratio of vehicles that cross the region's boundary with respect to their final destination. Moving towards the end of simulation, as expected $\eta^J_{IJ}(t)$ approaches to 1 indicating that all vehicles accumulating in the region's boundary have destinations in the other region.

The results of implementing the four control scenarios (a)–(d) are exhibited in Fig. 5 where the time-varying subregion accumulations $n_i(t)$ over the studied period are depicted. The LQR controller with dynamic cordon leads to border switching 18 times at time-steps $k_{\rho_s} = \{22, \ldots, 261\}$ [min]. The BB controller with dynamic cordon also leads to 18 times switching at $k_{\rho_s} = \{30, \ldots, 115\}$. It is apparent that the LQR control strategy (Fig. 5 (b,d)) outperformed the BB controller (Fig. 5 (a,c)) in both static and dynamic cordon scenarios, in a way that the BB controller resulted in the gridlock of Subregions 13 and 19 under conventional static cordon control scheme, resulting in a protracted hypercongestion. The proposed cordon selection algorithm applied every $\kappa = 5$ steps has

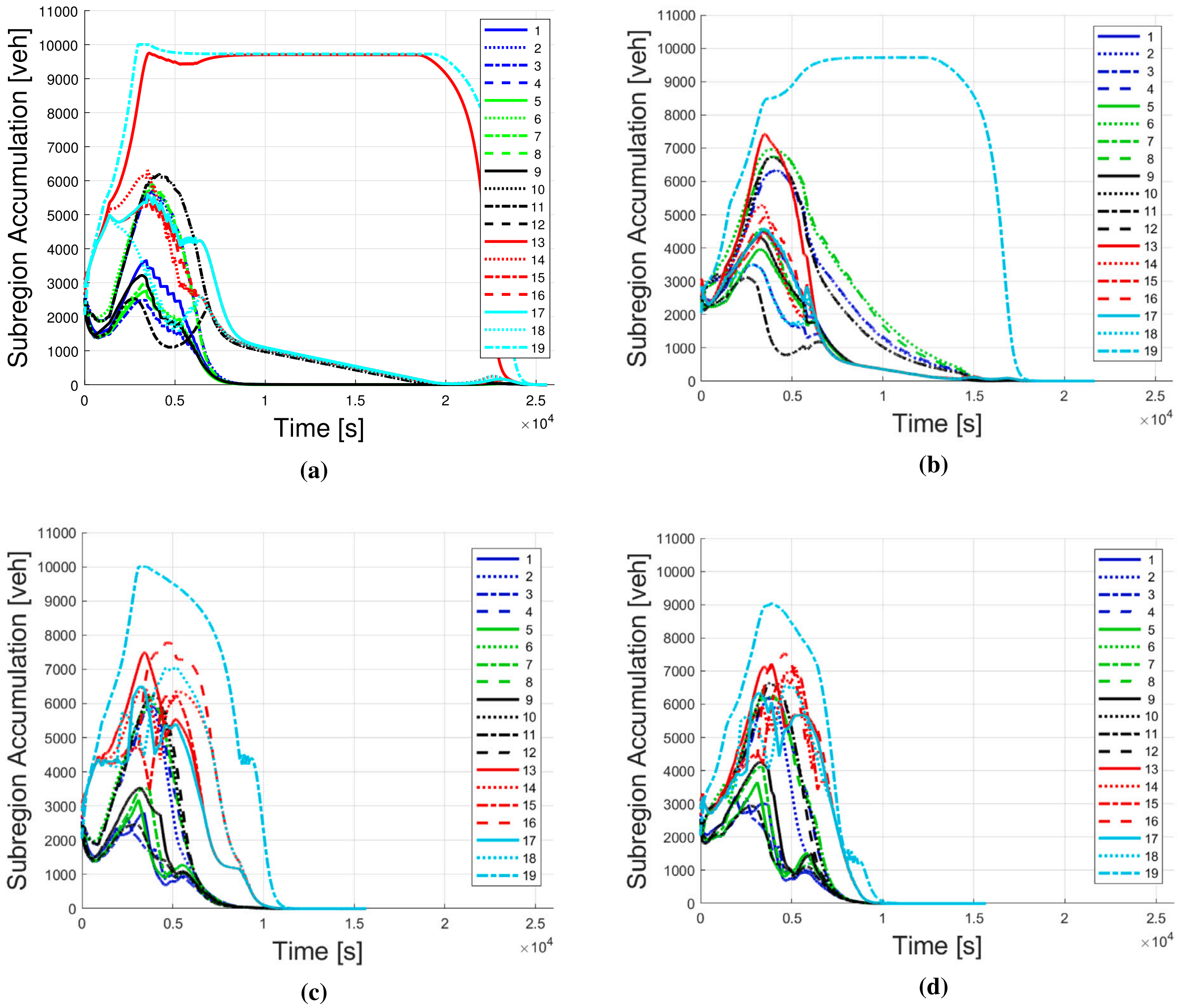

Fig. 5. Subregions' accumulations with: (a) BB + static cordon; (b) LQR + static cordon; (c) BB + dynamic cordon ($\kappa = 5$); and (d) LQR + dynamic cordon ($\kappa = 5$). The proposed LQR + dynamic cordon method results in a more homogeneous accumulation distribution in the whole network as well as shorter network clearance time compared to the other control strategies.

significantly improved the BB strategy to recover the network from the heavy congestion experienced in Subregion 13 where the network has fully cleared after 12600 [s] (see Fig. 5(c)). Note that the accumulation in each subregion does not exceed the jam accumulation, i.e. 10000 [veh], due to the receiving capacity function integrated into the subregion-level model (see Eq. (2)). The cordon changing algorithm has also significantly improved the performance of the LQR controller as delineated in Figs. 5(b) and 5(d). It can be seen that the network's accumulation is more evenly distributed across subregions (as the accumulation differences among subregions are smaller), and the network is cleared after 10500 [s] compared to 18500 [s] with static cordon.

A crucial hyper-parameter that should be appropriately adjusted to maximize the performance of the perimeter control methods with dynamic cordon is the switching interval κ. There is an optimum switching interval that results in the best performance of the LQR controller. This corresponds to the minimum switching interval that provides a sufficiently large interval for the linear optimal controller to regulate the network density. Table 1 summarizes the total time spent (TTS) [veh s] in the network as a result of implementing various control strategies with fixed and location-varying cordons and multiple switching intervals ($\kappa \in \{4, 5, 7, 10\}$) for the entire simulation period. It can be seen that the LQR controller with dynamic cordon and $\kappa = 5$ achieves the best performance among all the control algorithms, in a way that it lowers the TTS by over 57% with respect to the no-control scenario. Furthermore, implementing the cordon switching scheme with $\kappa = 5$ has reduced the TTS in the network by approximately 39% and 18% with respect to the static cordon counterparts of the BB and LQR gating schemes, respectively.

Fig. 6 visualizes congestion propagation through the network over time and over subregions, as well as the perimeter control cordon locations, when implementing the LQR controller empowered by the location-varying cordon ($\kappa = 5$). Note that the cordon selection algorithm ensures the connectivity of regions, in which case at most one subregion can be reallocated to a different region at every κ time-steps. Fig. 6 shows that Region 2 is compact while Region 1 is not which causes vehicles from Region 1 to Region 1

Table 1
Total time spent (expressed in [10^8 veh s]) in the network when implementing various control strategies. Note that the *no-control* strategy has resulted in the network gridlock. The numbers in parenthesis indicate the relative reduction in TTS against the no-control scenario.

Switching interval (κ)	Static cordon	Dynamic cordon			
	–	4	5	7	10
No control	12.25	–	–	–	–
Bang–bang	8.71 (−28.9%)	5.50 (−55.1%)	5.33 (−56.5%)	6.18 (−49.6%)	6.34 (−48.2%)
LQR	6.81 (−44.4%)	5.38 (−56.1%)	5.26 (−57.1%)	5.60 (−54.3%)	6.21 (−49.3%)

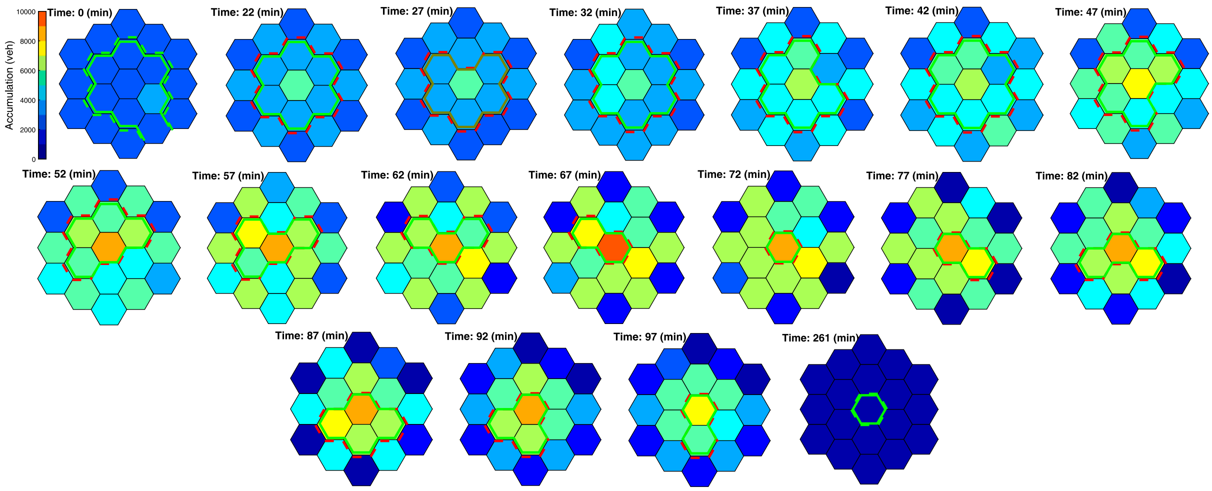

Fig. 6. Snapshots of subregions' accumulations over time when implementing the LQR controller with dynamic cordon algorithm ($\kappa = 5$). Each snapshot corresponds to a cordon switching instant during the simulation. The border of the regions and the magnitude of perimeter control outputs in each snapshot is demonstrated by a dashed line ($U_{12}(t)$) and a solid line ($U_{21}(t)$). The colour of the dashed and solid lines respectively indicate the relative magnitude, with red and green corresponding to $U^{\min}$ and $U^{\max}$, respectively. The colorbar indicates the level of accumulation in each subregion. (For interpretation of the colours in this figure, the reader is referred to the web version of the manuscript).

to possibly cross the region boundary more than one time, and hence this should be carefully considered in the region-level model (see definition of Θ in Eq. (6)). Each subfigure delineates the spatial distribution of the accumulation at a certain switching instance, till the network is cleared. The figure shows that congestion initially sparks in three central subregions (13, 14, and 19), and then it spreads to other subregions. Due to the effective spatial and temporal border switching, vehicles are more uniformly distributed across the subregions throughout the simulation. The congestion starts to diminish after 87 [min], whereas the cordon selection algorithm transfers the most congested subregions to Region 2. Note that the dynamic cordon feature of the perimeter controller ensures Subregion 19 becomes directly controllable early on to protect it from hypercongestion, whereas the LQR with static cordon controller fails to achieve this.

Applied perimeter control outputs obtained from the four scenarios are depicted in Fig. 7. The control outputs with static cordon (Fig. 7(a,b)) frequently fluctuate compared against the controllers with dynamic cordon (Fig. 7(c,d)). In particular, between $t = 2000$ [s] and $t = 6000$ [s], which is the most congested period, the control outputs with dynamic cordon strategies are often operated at $U_{12}(t) = U^{\min} = 0.1$ and $U_{21}(t) = U^{\max} = 0.9$, i.e. minimizing the traffic inflow into Region 2 and maximizing it to Region 1. This observation emphasizes that the cordon switching algorithm systematically and effectively identifies and protects the most congested subregions in real-time. On the contrary, the static cordon strategy lacks this feature, and thus both control scenarios are obliged to completely (for BB) or partially (for LQR) open up the gated transfer flow to Region 2, whenever the overall accumulation of the Region 1 exceeds a certain level of congestion. On these occasions, the optimal LQR controller still has the advantage of using the full range of the control output spectrum, while the BB controller has to minimize $U_{21}(t)$ and maximize $U_{12}(t)$ since both regions are congested (see Section 4.1).

The regional accumulations and production MFDs are shown in Fig. 8 and Fig. 9, respectively. These figures provide a region-level view of the network performance when applying the four control scenarios. Fig. 8(a) shows both regions are cleared at the very end of simulation (i.e. 25000 [s]) by implementing the BB control algorithm with a static cordon, whereas the dynamic cordon strategy clears the network after 11000 [s] (see Fig. 8(c)). The key difference between the two strategies can be sought from the subregion accumulation dynamics in Fig. 5 and control outputs in Fig. 7 showing that Subregions 13 and 19 are better protected with the dynamic cordon. Moreover, comparing the two alternative cordon control plans further highlights the dynamic cordon control leads to a higher accumulation of Region 1 because more subregions are allocated to Region 1. Further, the dynamic cordon results in jumps in the regional accumulation due to switching subregions, as shown in Figs. 8(c) and 8(d). At around 5000 [s],

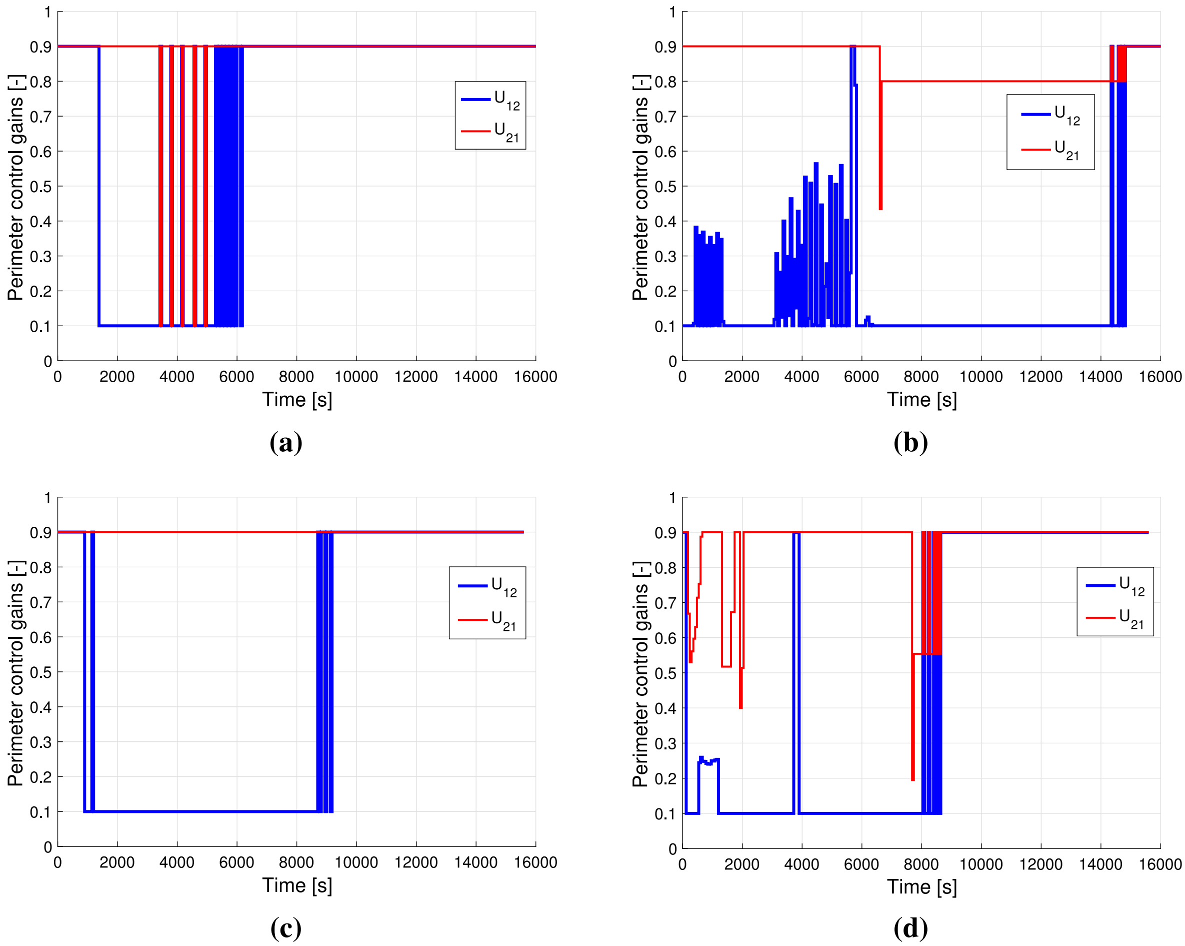

Fig. 7. Perimeter control outputs during the simulation period when applying the following control strategies: (a) BB + static cordon; (b) LQR + static cordon; (c) BB + dynamic cordon ($\kappa = 5$); and (d) LQR + dynamic cordon ($\kappa = 5$).

the accumulation in Region 2 declines as a result of cordon changes such that Region 2 includes only Subregion 19, (see Fig. 6). Thereafter, Region 2 accumulation increases because more subregions are allocated to Region 2. The effect of location-varying cordon is more clearly demonstrated in Fig. 9, where each switching shows itself as a discontinuity (jump) in the MFD of each region. The hysteresis loops are observed in the static cordon scenarios, as shown in Fig. 9(a, b), whereas the dynamic cordon is capable to reduce the hysteresis in Region 1 (see Fig. 9(c, d)). Since the number of subregions change significantly in Region 2 (from 7 subregions to only 1), the jumps in its MFD are more apparent compared to Region 1. Fig. 9 further demonstrates that the modelled MFDs (i.e. dashed lines) can track the plant MFDs (i.e. solid lines) accurately. Overall the proposed perimeter controller is efficient and capable of handling errors due to the aggregation (loss of detailed information) of dynamics from subregion to region level, as well as the linearization approximations.

5. Summary and future research

A perimeter control method with location-varying cordon has been proposed and its effectiveness in reducing congestion in a heterogeneous large-scale urban network has been demonstrated. The location-varying cordon selection algorithm has enabled effective management of spatial and temporal heterogeneity of demand and propagation of congestion by recurrently allocating uncongested subregions to the peripheral region and concentrating congested subregions into the protected region. Consistent region-level and subregion-level traffic models of the network have been derived based on MFD dynamics. The models assume that vehicles can cross the region boundaries multiple times. An optimal LQR scheme has been developed based on the linearized switching model of the network. The model incorporates the impacts of MFD hysteresis phenomena governed by the underlying heterogeneous density distribution across the network.

The LQR theory has been applied to obtain the optimal control inputs of the perimeter control for a two-region network comprising 19 homogeneous subregions subject to an imbalanced morning peak-hour demand profile. Results pinpoint the cordon

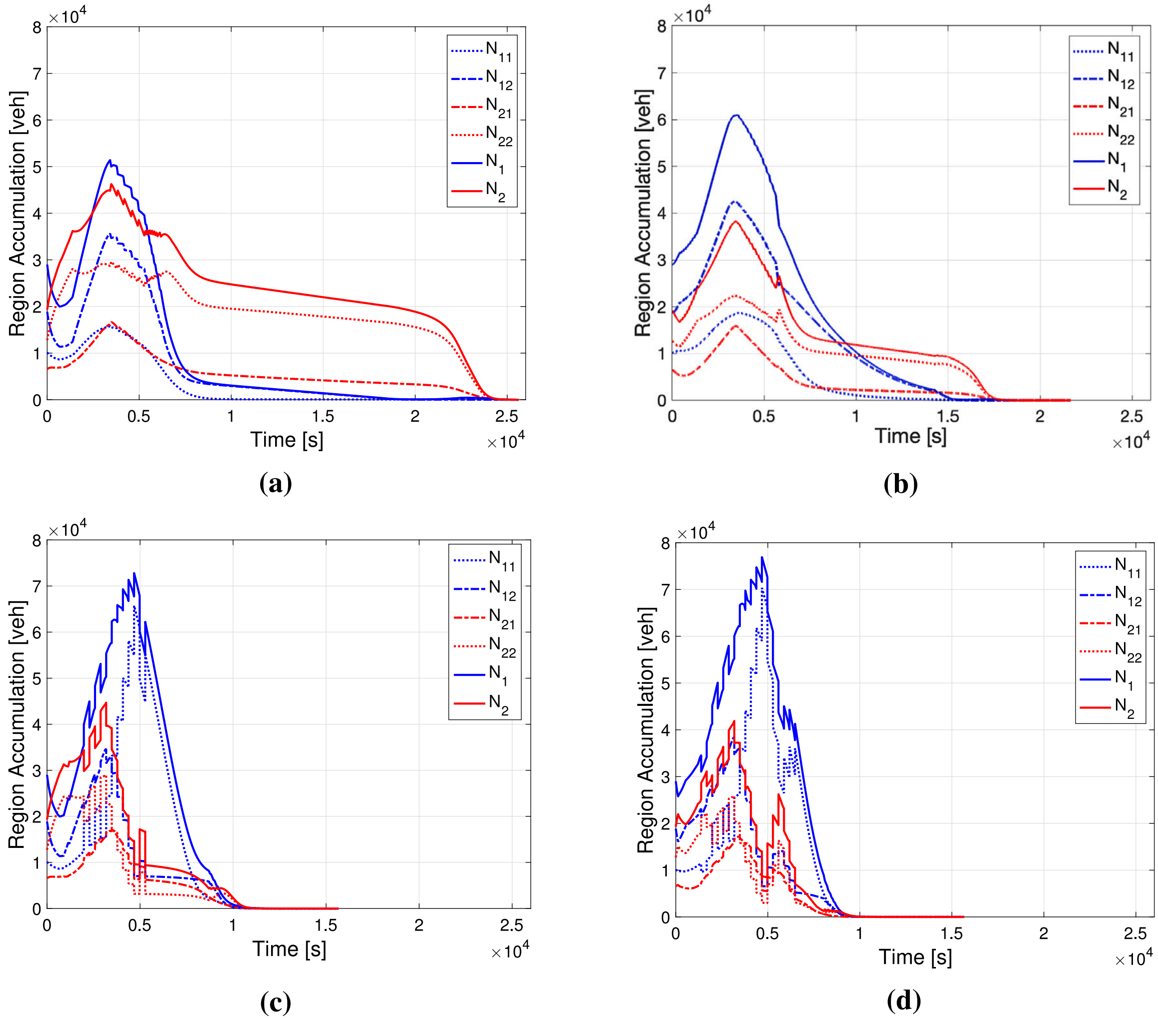

Fig. 8. Regional accumulations during the simulation period when applying the following control strategies: (a) BB + static cordon; (b) LQR + static cordon; (c) BB + dynamic cordon ($\kappa = 5$); and (d) LQR + dynamic cordon ($\kappa = 5$). In the dynamic cordon scenarios, the accumulation in Region 2 reduces around time 5000 [s] because of the location-varying cordon that only Subregion 19 is in Region 2. Then the accumulation increases since more subregions are added to Region 2, see Fig. 6.

switching strategy is a powerful add-on to the region-level gating schemes in balancing the regions accumulations and protecting the subregions that are prone to hypercongestion.

Several future research directions are envisaged. In the early stages of traffic automation, when there is a mixture of autonomous and human-driven vehicles, the perimeter control and cordon selection algorithm both can adapt to the potential influence of autonomous vehicles on each subregion's capacity and the boundary capacity between subregions (see e.g. Mohajerpoor and Ramezani (2019)). Moreover, the proposed dynamic cordon approach provides greater potential in congestion management such as congestion pricing with a time-varying cordon. In addition, the network can be extended to include multiple modes of transport including public transport, which underpins the application of multi-modal MFDs. Furthermore, another future research direction is to apply the proposed cordon selection algorithm to a traffic microsimulation model, and tackling the local spillbacks at the controlled intersections.

CRediT authorship contribution statement

Ye Li: Methodology, Software, Validation, Formal analysis, Investigation, Data curation, Writing - original draft, Writing - review & editing. **Reza Mohajerpoor:** Methodology, Software, Validation, Formal analysis, Investigation, Writing - original draft, Writing - review & editing. **Mohsen Ramezani:** Conceptualization, Methodology, Validation, Formal analysis, Investigation, Resources, Writing - original draft, Writing - review & editing, Supervision.

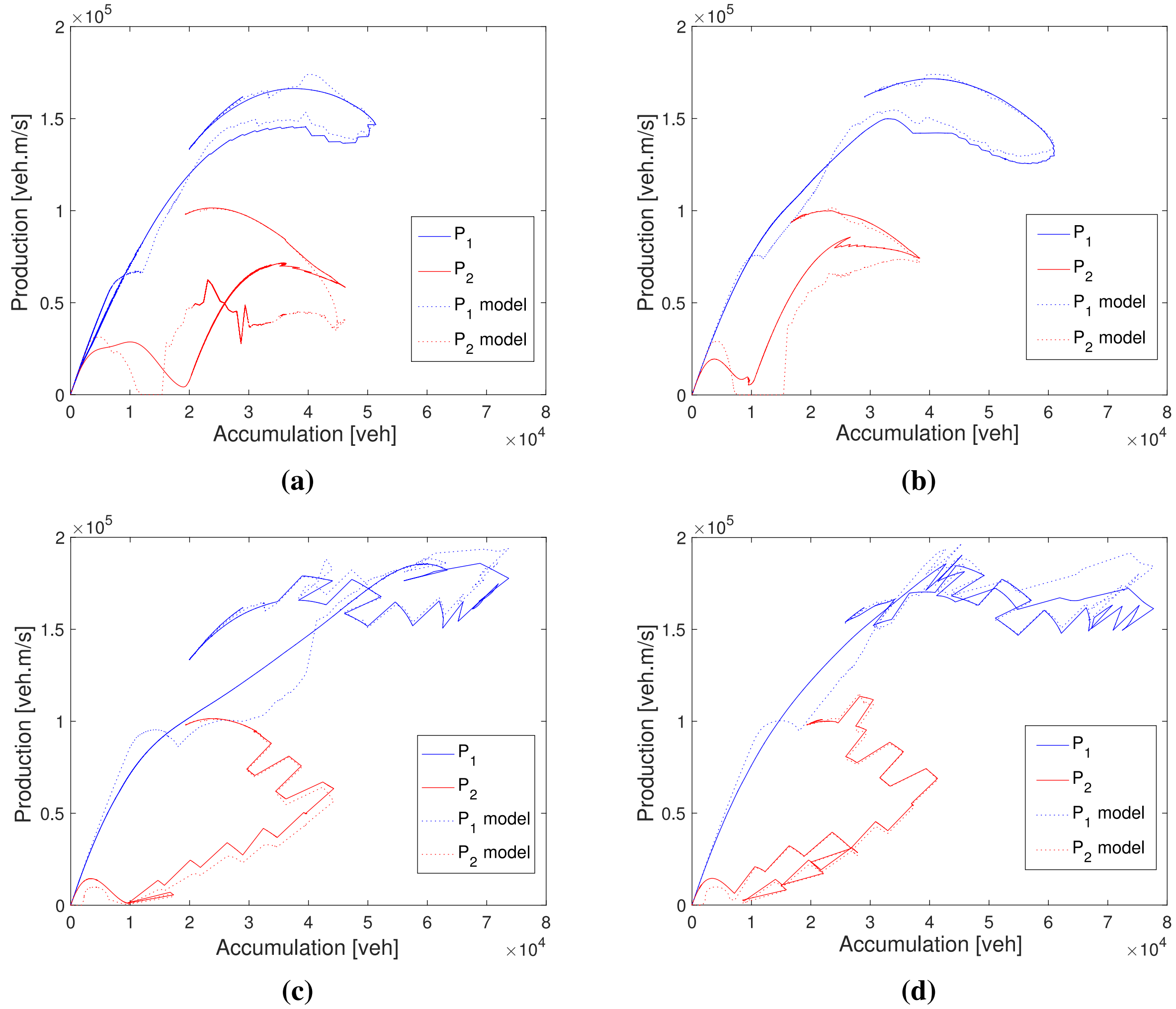

Fig. 9. Production MFDs obtained from simulations when applying the following control strategies: (a) BB + static cordon; (b) LQR + static cordon; (c) BB + dynamic cordon ($\kappa = 5$); and (d) LQR + dynamic cordon ($\kappa = 5$). Note that P_1 and P_2 represent actual production MFDs obtained from the subregion-level model, and they are compared against those estimated from Eq. (5). Note that a subregion might transfer to a different region over time due to the cordon switching, resulting in jumps in MFDs with dynamic cordon.

Appendix A. Nomenclature

Notation	Description
$\|\mathcal{X}\|$	Cardinality (or size) of Set $\mathcal{X}$
$\mathbb{R}^n$	The n-dimensional Euclidean space
$\mathbb{R}^{n\times m}$	The space of $n \times m$ dimensional real matrices
$\mathbb{S}^{n\times n}$	The space of $n \times n$ dimensional real symmetric matrices
$\mathcal{R}$	Set of subregions in the network
$\|\mathcal{R}\|$	Total number of subregions in the network
$\mathcal{R}_I(t)$	Set of subregions in Region I at time t
$\mathcal{R}_I^*(t)$	New set of subregions in Region I at time t
$\|\mathcal{R}_I(t)\|$	Number of subregions in Region I at time t
ϕ_i	Set of subregions adjacent to Subregion i
$p_i(n_i(t))$ [veh m/s]	Production MFD of Subregion i with accumulation n_i at time t
$p^{\max}(n_i^{\mathrm{cr}})$ [veh m/s]	Maximum of production MFD of Subregion i
d_{3i}, d_{2i}, d_{1i}	Parameters of Subregion i MFD

Notation	Description
$\tilde{D}_{3I}$, $\tilde{D}_{2I}$, $\tilde{D}_{1I}$, D_{σ_I}, β_I	Constant scalar parameters of Region I MFD
$n_i(t)$ [veh]	Accumulation of Subregion i at time t
$n_{ij}(t)$ [veh]	Accumulation in Subregion i with destinations in Subregion j at time t
n_i^{cr} [veh]	Critical accumulation of Subregion i
n_i^{jam} [veh]	Jam accumulation of Subregion i
$q_{ij}(t)$ [veh/s]	Exogenous travel demand generated in Subregion i with destination in Subregion j at time t
b_{ih} [veh/s]	Fixed boundary capacity between Subregion i and Subregion h
$r_h(n_h(t))$ [veh/s]	Receiving capacity of Subregion h with accumulation n_h at time t
$r_h^{\max}$ [veh/s]	Maximum receiving capacity of Subregion h
$m_{ij}^h(t)$ [veh/s]	Demand for transfer outflow from Subregion i with destination in Subregion j through immediate Subregion h at time t
$\hat{m}_{ij}^h(t)$ [veh/s]	Realized transfer outflow from Subregion i with destination in Subregion j through immediate Subregion h at time t
$u_{ij}(t)$	Perimeter control output between Subregion i and Subregion j at time t
$\theta_{ij}^h(t)$	Proportion of vehicles in Subregion i with destination Subregion j that pass through Subregion h at time t
$w_i(t)$	Density weight of Subregion i at time t
$s_i(t)$	Sending outflow pressure of Subregion i at time t
$\lambda_i(t)$	Protection index of Subregion i
τ [s]	Common cycle time of controlled cordon intersections, which is the sample time of the discretized dynamic model of the network
κ	Switching interval, or the minimum number of time-steps that the cordon does not switch after a switching occurred
$N_I(t)$ [veh]	Number of vehicles in Region I at time t
$N_{II}(t)$ [veh]	Number of vehicles in Region I with final destination in Region I at time t
$N_{IJ}(t)$ [veh]	Number of vehicles in Region I with destination Region J at time t
$Q_{II}(t)$ [veh/s]	Travel demand generated in Region I with final destination of Region I at time t
$Q_{IJ}(t)$ [veh/s]	Travel demand generated in Region I with destination Region J at time t
$M_{II}^I(t)$ [veh/s]	Internal outflow from Region I with destination of Region I through Region I at time t
$M_{IJ}^H(t)$ [veh/s]	External outflow from Region I with destination Region J that passes through Region H at time t
$U_{IJ}(t)$	Perimeter control output between Region I and Region J at time t
$\Theta_{IJ}^H(t)$	Proportion of vehicles in Region I with destination Region J that pass through Region H at time t
$\eta_{II}^J(t)$	Proportion of transfer flows that pass the boundary between Region I and Region J at time t immediately (without travel through series of subregions in their departure region) with final destination in Region I
$\eta_{IJ}^J(t)$	Proportion of transfer flows that pass the boundary between Region I and Region J at time t immediately (without travel through series of subregions in their departure region) with final destination in Region J
$L_{II}(t)$ [m]	Average trip length of trips from Region I to Region I at time t
$L_{IJ}(t)$ [m]	Average trip length of trips from Region I to Region J at time t
$P_I(N_I(t))$ [veh m/s]	Production MFD for Region I with accumulation N_I at time t
$\sigma(N_I(t))$ [veh]	Standard deviation of accumulations among all links in Region I
$N_{I,\rho_s}^{\mathrm{jam}}$ [veh]	Jam accumulation in Region I for the network at switching state ρ_s
σ_I^{het} [veh]	Standard deviation of $\|\mathscr{R}_I(t)\|$ negative binomial distributions with mean density of $N_I(t)$ / $\|\mathscr{R}_I(t)\|$
$\bar{\Lambda}_I(t)$	Average protection index for Region I at time t
$U^{\min}$ and $U^{\max}$	Lower and upper bounds of perimeter control outputs
A_{ρ_s}, B_{ρ_s} and D_{ρ_s}	Constant matrices that characterize the linearized discrete-time accumulation dynamics of the network at switching state ρ_s
K_{ρ_s}	Constant control gain of the network at switching state ρ_s

Appendix B. Descriptions of linearized matrices A_{ρ_s} and B_{ρ_s}

Linearizing Eq. (7) with respect to the SS demand, accumulations, and control outputs at the switched state ρ_s, results in the following dynamic equations:

$$\Delta \dot{N}_{\rho_s}(t) = \tilde{A}_{\rho_s}\Delta N_{\rho_s}(t) + \tilde{B}_{\rho_s}\Delta U_{\rho_s}(t) + \Delta Q_{\rho_s}(t) + \tilde{\mathbf{O}}\left(\Delta L_{\rho_s}(t), \Delta\Theta_{\rho_s}(t), \Delta\eta_{\rho_s}(t)\right), \tag{B.1}$$

where $\tilde{A}_{\rho_s}$ and $\tilde{B}_{\rho_s}$ are defined below. Discretization of Eq. (B.1) results in Eq. (16) with $A_{\rho_s} = (I_{s_n} + \tau\tilde{A}_{\rho_s})$, $B_{\rho_s} = \tau\tilde{B}_{\rho_s}$, and $D_{\rho_s} = \tau I_{s_n}$. Let us define
$\tilde{F}_I(N^*_{I,\rho_s}, \sigma(N^*_{I,\rho_s})) \triangleq (2\tilde{D}_{3I}N^*_{I,\rho_s} + \tilde{D}_{2I})(D_{\sigma_I}e^{\beta_I(\sigma_I(N^*_{I,\rho_s})-\sigma^{\text{het}}_{I,\rho_s})} + (1-D_{\sigma_I})) + \left(\tilde{D}_{3I}N^{*2}_{I,\rho_s} + \tilde{D}_{2I}N^*_{I,\rho_s} + \tilde{D}_{1I}\right)\beta_I D_{\sigma_I}\partial\sigma_I(N^*_{I,\rho_s})e^{\beta_I(\sigma_I(N^*_{I,\rho_s})-\sigma^{\text{het}}_{I,\rho_s})}$, and $N^{\text{jam}}_I\partial\sigma_I(N^*_I) \triangleq 3\chi^*_{3I}(N^*_I/N^{\text{jam}}_I)^2 + 2\chi^*_{2I}(N^*_I/N^{\text{jam}}_I) + \chi^*_{1I}$, $P^*_{I,\rho_s} \triangleq P_I(N^*_{I,\rho_s}, \sigma(N^*_{I,\rho_s}))$, and $\tilde{F}^*_{I,\rho_s} \triangleq \tilde{F}_I(N^*_{I,\rho_s}, \sigma(N^*_{I,\rho_s}))$, $I \in \{1,2\}$. Thereupon, we have $\tilde{A}_{\rho_s} = \left[\tilde{A}_{ij,\rho_s}\right]$, $\tilde{B}_{\rho_s} = \left[\tilde{B}_{ik,\rho_s}\right]$, $i,j \in \{1,\dots,4\}$, and $k \in \{1,2\}$, wherein the elements are defined in the sequel:

$$\begin{aligned}
\tilde{A}_{11,\rho_s} &= -\Theta^{1*}_{11,\rho_s}\left(\frac{N^*_{11,\rho_s}}{L^*_{11,\rho_s}}\tilde{F}^*_{1,\rho_s} + \frac{P^*_{1,\rho_s}}{N^*_{1,\rho_s}L^*_{11,\rho_s}}\right) - U^*_{12,\rho_s}\Theta^{2*}_{11,\rho_s}\eta^{2*}_{11,\rho_s}\left(\frac{N^*_{11,\rho_s}}{L^*_{12,\rho_s}}\tilde{F}^*_{1,\rho_s} + \frac{P^*_{1,\rho_s}}{N^*_{1,\rho_s}L^*_{12,\rho_s}}\right),\\
\tilde{A}_{12,\rho_s} &= -U^*_{12,\rho_s}\Theta^{2*}_{11,\rho_s}\eta^{2*}_{11,\rho_s}\frac{N^*_{11,\rho_s}}{L^*_{12,\rho_s}}\tilde{F}^*_{1,\rho_s} - \Theta^{1*}_{11,\rho_s}\frac{N^*_{11,\rho_s}}{L^*_{11,\rho_s}}\tilde{F}^*_{1,\rho_s},\\
\tilde{A}_{13,\rho_s} &= U^*_{21,\rho_s}\Theta^{1*}_{21,\rho_s}\eta^{1*}_{21,\rho_s}\left(\frac{N^*_{21,\rho_s}}{L^*_{21,\rho_s}}\tilde{F}^*_{2,\rho_s} + \frac{P^*_{2,\rho_s}}{N^*_{2,\rho_s}L^*_{21,\rho_s}}\right),\\
\tilde{A}_{14,\rho_s} &= U^*_{21,\rho_s}\Theta^{1*}_{21,\rho_s}\eta^{1*}_{21,\rho_s}\frac{N^*_{21,\rho_s}}{L^*_{21}}\tilde{F}^*_{2,\rho_s},\\
\tilde{A}_{21,\rho_s} &= -U^*_{12,\rho_s}\Theta^{2*}_{12,\rho_s}\eta^{2*}_{12,\rho_s}\frac{N^*_{12,\rho_s}}{L^*_{12,\rho_s}}\tilde{F}^*_{1,\rho_s},\\
\tilde{A}_{22,\rho_s} &= -U^*_{12,\rho_s}\Theta^{2*}_{12,\rho_s}\eta^{2*}_{12,\rho_s}\left(\frac{N^*_{12,\rho_s}}{L^*_{12,\rho_s}}\tilde{F}^*_{1,\rho_s} + \frac{P^*_{1,\rho_s}}{N^*_{1,\rho_s}L^*_{12,\rho_s}}\right),\\
\tilde{A}_{23,\rho_s} &= U^*_{21,\rho_s}\Theta^{1*}_{22,\rho_s}\eta^{1*}_{22,\rho_s}\frac{N^*_{22,\rho_s}}{L^*_{21,\rho_s}}\tilde{F}^*_{2,\rho_s},\\
\tilde{A}_{24,\rho_s} &= U^*_{21,\rho_s}\Theta^{1*}_{22,\rho_s}\eta^{1*}_{22,\rho_s}\left(\frac{N^*_{22,\rho_s}}{L^*_{21,\rho_s}}\tilde{F}^*_{2,\rho_s} + \frac{P^*_{2,\rho_s}}{N^*_{2,\rho_s}L^*_{21}}\right),\\
\tilde{A}_{31,\rho_s} &= U^*_{12,\rho_s}\Theta^{2*}_{11,\rho_s}\eta^{2*}_{11,\rho_s}\left(\frac{N^*_{11,\rho_s}}{L^*_{12,\rho_s}}\tilde{F}^*_{1,\rho_s} + \frac{P^*_{1,\rho_s}}{N^*_{1,\rho_s}L^*_{12,\rho_s}}\right),\\
\tilde{A}_{32,\rho_s} &= U^*_{12,\rho_s}\Theta^{2*}_{11,\rho_s}\eta^{2*}_{11,\rho_s}\frac{N^*_{11,\rho_s}}{L^*_{12,\rho_s}}\tilde{F}^*_{1,\rho_s},\\
\tilde{A}_{33,\rho_s} &= -U^*_{21,\rho_s}\Theta^{1*}_{21,\rho_s}\eta^{1*}_{21,\rho_s}\left(\frac{N^*_{21,\rho_s}}{L^*_{21,\rho_s}}\tilde{F}^*_{2,\rho_s} + \frac{P^*_{2,\rho_s}}{N^*_{2,\rho_s}L^*_{21,\rho_s}}\right),\\
\tilde{A}_{34,\rho_s} &= -U^*_{21,\rho_s}\Theta^{1*}_{21,\rho_s}\eta^{1*}_{21,\rho_s}\frac{N^*_{21,\rho_s}}{L^*_{21,\rho_s}}\tilde{F}^*_{2,\rho_s},\\
\tilde{A}_{41,\rho_s} &= U^*_{12,\rho_s}\Theta^{2*}_{12,\rho_s}\eta^{2*}_{12,\rho_s}\frac{N^*_{12,\rho_s}}{L^*_{12,\rho_s}}\tilde{F}^*_{1,\rho_s},\\
\tilde{A}_{42,\rho_s} &= U^*_{12,\rho_s}\Theta^{2*}_{12,\rho_s}\eta^{2*}_{12,\rho_s}\left(\frac{N^*_{12,\rho_s}}{L^*_{12,\rho_s}}\tilde{F}^*_{1,\rho_s} + \frac{P^*_{1,\rho_s}}{N^*_{1,\rho_s}L^*_{12,\rho_s}}\right),\\
\tilde{A}_{43,\rho_s} &= -U^*_{21,\rho_s}\Theta^{1*}_{22,\rho_s}\eta^{1*}_{22,\rho_s}\frac{N^*_{22,\rho_s}}{L^*_{21,\rho_s}}\tilde{F}^*_{2,\rho_s} - \Theta^{2*}_{22,\rho_s}\frac{N^*_{22,\rho_s}}{L^*_{22,\rho_s}}\tilde{F}^*_{2,\rho_s},\\
\tilde{A}_{44,\rho_s} &= -\Theta^{2*}_{22,\rho_s}\left(\frac{N^*_{22,\rho_s}}{L^*_{22,\rho_s}}\tilde{F}^*_{2,\rho_s} + \frac{P^*_{2,\rho_s}}{N^*_{2,\rho_s}L^*_{22,\rho_s}}\right) - U^*_{21,\rho_s}\Theta^{1*}_{22,\rho_s}\eta^{1*}_{22,\rho_s}\left(\frac{N^*_{22,\rho_s}}{L^*_{21,\rho_s}}\tilde{F}^*_{2,\rho_s} + \frac{P^*_{2,\rho_s}}{N^*_{2,\rho_s}L^*_{21,\rho_s}}\right),\\
\tilde{B}_{11,\rho_s} &= -\Theta^{2*}_{11,\rho_s}\eta^{2*}_{11,\rho_s}N^*_{11,\rho_s}\frac{P^*_{1,\rho_s}}{N^*_{1,\rho_s}L^*_{12,\rho_s}},\ \tilde{B}_{12,\rho_s} = \Theta^{1*}_{21,\rho_s}\eta^{1*}_{21,\rho_s}N^*_{21,\rho_s}\frac{P^*_{2,\rho_s}}{N^*_{2,\rho_s}L^*_{21,\rho_s}},\\
\tilde{B}_{21,\rho_s} &= -\Theta^{2*}_{12,\rho_s}\eta^{2*}_{12,\rho_s}N^*_{12,\rho_s}\frac{P^*_{1,\rho_s}}{N^*_{1,\rho_s}L^*_{12,\rho_s}},\ \tilde{B}_{22,\rho_s} = \Theta^{1*}_{22,\rho_s}\eta^{1*}_{22,\rho_s}N^*_{22,\rho_s}\frac{P^*_{2,\rho_s}}{N^*_{2,\rho_s}L^*_{21,\rho_s}},\\
\tilde{B}_{31,\rho_s} &= -\tilde{B}_{11,\rho_s},\ \tilde{B}_{32,\rho_s} = -\tilde{B}_{12,\rho_s},\ \tilde{B}_{41,\rho_s} = -\tilde{B}_{21,\rho_s},\ \text{and}\ \tilde{B}_{42,\rho_s} = -\tilde{B}_{22,\rho_s}.
\end{aligned}$$

Appendix C. Estimating region accumulation STD

Given that the network at the subregion level pertains homogeneous MFD characteristics, it has been shown using empirical data (Geroliminis and Sun, 2011) that the accumulation STD of each subregion can be estimated by a unimodal 3rd degree polynomial function of the subregion's normalized accumulation (i.e. accumulation over jam accumulation):

$$\sigma(n_i(t)) = \alpha_{\sigma_{3i}}\left(\frac{n_i(t)}{n_i^{\text{jam}}}\right)^3 + \alpha_{\sigma_{2i}}\left(\frac{n_i(t)}{n_i^{\text{jam}}}\right)^2 + \alpha_{\sigma_{1i}}\left(\frac{n_i(t)}{n_i^{\text{jam}}}\right), \tag{C.1}$$

where n_i^{jam} is the jam accumulation of Subregion $i \in \mathscr{R}$ and $\alpha_{\sigma_{mi}}$, $m \in \{1,2,3\}$, are scalar parameters that can be obtained from the historical links' accumulations in the subregion (see Figure 4 in (Geroliminis and Sun, 2011)).

To scale this up at the region level, a well-defined function as Eq. (C.1) cannot be defined due to the density heterogeneity of the network. By plotting the STD versus mean occupancy of the network as demonstrated in Fig. C.10, it is clear that the network's STD

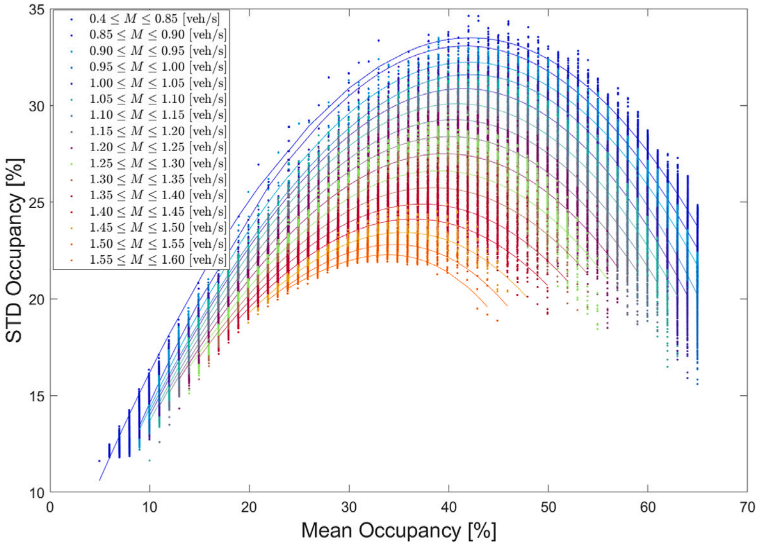

Fig. C.10. Equioutflow lines in the average occupancy vs. STD occupancy plane. Each solid line represents the variation of the STD of density with respect to the average density for a network with outflow constrained to a certain bin. In this figure, M represents the total outflow of the network. The data for this figure is obtained as Figure 4 in Ramezani et al. (2015).

occupancy may not be uniquely defined by its mean occupancy. However, the figure highlights that the STD and mean occupancy are strongly correlated through production, in a way that a well-defined 3rd order polynomial can fit to the data given a *certain* outflow. Conclusively, the occupancy STD can be uniquely defined as a function of the mean occupancy and outflow:

$$\sigma(N_{I,\rho_s}(t)) = \chi_{3I,\rho_s}(t)\left(\frac{N_{I,\rho_s}(t)}{N^{\text{jam}}_{I,\rho_s}}\right)^3 + \chi_{2I,\rho_s}(t)\left(\frac{N_{I,\rho_s}(t)}{N^{\text{jam}}_{I,\rho_s}}\right)^2 + \chi_{1I,\rho_s}(t)\left(\frac{N_{I,\rho_s}(t)}{N^{\text{jam}}_{I,\rho_s}}\right), \tag{C.2}$$

where $N^{\text{jam}}_{I,\rho_s}$ is the jam density of Region I, and $\chi_{mI,\rho_s}(t) = \chi_{mI,\rho_s}(P_{I,\rho_s}(t))$, $m \in \{1,2,3\}$ are scalar functions that are acquired from the comprehended data regression process. At a switching instance, the nominal χ^*_{mI,ρ_s} parameters are identified by finding the best polynomial (among all polynomials shown in Fig. C.10) that fits to the nominal accumulation (N^*_{I,ρ_s}) and STD occupancy ($\sigma(N^*_{I,\rho_s})$).

References

Aalipour, A., Kebriaei, H., Ramezani, M., 2018. Analytical optimal solution of perimeter traffic flow control based on mfd dynamics: a pontryagin's maximum principle approach. IEEE Trans. Intell. Transp. Syst. 20 (9), 3224–3234.
Aghamohammadi, R., Laval, J.A., 2020. A continuum model for cities based on the macroscopic fundamental diagram: A semi-Lagrangian solution method. Transp. Res. B 132 (C), 101–116.
Amirgholy, M., Gao, H.O., 2017. Modeling the dynamics of congestion in large urban networks using the macroscopic fundamental diagram: User equilibrium, system optimum, and pricing strategies. Transp. Res. B 104, 215–237.
Ampountolas, K., Zheng, N., Geroliminis, N., 2017. Macroscopic modelling and robust control of bi-modal multi-region urban road networks. Transp. Res. B 104, 616–637.
Anderson, B.D., Moore, J.B., 2007. Optimal Control: Linear Quadratic Methods. Courier Corporation.
Csikós, A., Charalambous, T., Farhadi, H., Kulcsár, B., Wymeersch, H., 2017. Network traffic flow optimization under performance constraints. Transp. Res. C 83, 120–133.
Daganzo, C.F., Lehe, L.J., 2015. Distance-dependent congestion pricing for downtown zones. Transp. Res. B 75, 89–99.
Ding, H., Zhang, Y., Zheng, X., Yuan, H., Zhang, W., 2017. Hybrid perimeter control for two-region urban cities with different states. IEEE Trans. Control Syst. Technol. 26 (6), 2049–2062.
Ding, H., Zhou, J., Zheng, X., Zhu, L., Bai, H., Zhang, W., 2020. Perimeter control for congested areas of a large-scale traffic network: A method against state degradation risk. Transp. Res. C 112, 28–45.
Fu, Y., Li, S., Yang, L., 2020. Robust perimeter control design for two urban regions with sampled-data and input saturation. Transp. B Transp. Dynam. 1–23.
Gayah, V.V., Daganzo, C.F., 2011. Clockwise hysteresis loops in the macroscopic fundamental diagram: an effect of network instability. Transp. Res. B 45 (4), 643–655.
Geroliminis, N., Daganzo, C.F., 2008. Existence of urban-scale macroscopic fundamental diagrams: Some experimental findings. Transp. Res. B 42 (9), 759–770.
Geroliminis, N., Haddad, J., Ramezani, M., 2012. Optimal perimeter control for two urban regions with macroscopic fundamental diagrams: A model predictive approach. IEEE Trans. Intell. Transp. Syst. 14 (1), 348–359.
Geroliminis, N., Sun, J., 2011. Properties of a well-defined macroscopic fundamental diagram for urban traffic. Transp. Res. B 45 (3), 605–617.
Godfrey, J.W., 1969. Coordinated distributed adaptive perimeter control for large-scale urban road networks. Traffic Eng. Control 11, 323–327.
Gu, Z., Shafiei, S., Liu, Z., Saberi, M., 2018. Optimal distance-and time-dependent area-based pricing with the network fundamental diagram. Transp. Res. C 95, 1–28.

Guo, Q., Ban, X.J., 2020. Macroscopic fundamental diagram based perimeter control considering dynamic user equilibrium. Transp. Res. B 136, 87–109.
Haddad, J., 2015. Robust constrained control of uncertain macroscopic fundamental diagram networks. Transp. Res. C 59, 323–339.
Haddad, J., 2017. Optimal perimeter control synthesis for two urban regions with aggregate boundary queue dynamics. Transp. Res. B 96, 1–25.
Haddad, J., Mirkin, B., 2020. Resilient perimeter control of macroscopic fundamental diagram networks under cyberattacks. Transp. Res. B 132, 44–59.
Haddad, J., Zheng, Z., 2018. Adaptive perimeter control for multi-region accumulation-based models with state delays. Transp. Res. B.
Han, Y., Ramezani, M., Hegyi, A., Yuan, Y., Hoogendoorn, S., 2020. Hierarchical ramp metering in freeways: an aggregated modeling and control approach. Transp. Res. C 110, 1–19.
He, Q., Head, K.L., Ding, J., 2014. Multi-modal traffic signal control with priority, signal actuation and coordination. Transp. Res. C 46, 65–82.
Ingole, D., Mariotte, G., Leclercq, L., 2020. Perimeter gating control and citywide dynamic user equilibrium: a macroscopic modeling framework. Transp. Res. C 111, 22–49.
Keyvan-Ekbatani, M., Carlson, R.C., Knoop, V.L., Papageorgiou, M., 2021. Optimizing distribution of metered traffic flow in perimeter control: Queue and delay balancing approaches. Control Eng. Pract. 110, 104762.
Keyvan-Ekbatani, M., Gao, X., Gayah, V.V., Knoop, V.L., 2019. Traffic-responsive signals combined with perimeter control: investigating the benefits. Transp. B Transp. Dyn. 7 (1), 1402–1425.
Keyvan-Ekbatani, M., Yildirimoglu, M., Geroliminis, N., Papageorgiou, M., 2015. Multiple concentric gating traffic control in large-scale urban networks. IEEE Trans. Intell. Transp. Syst. 16 (4), 2141–2154.
Kouvelas, A., Saeedmanesh, M., Geroliminis, N., 2017. Enhancing model-based feedback perimeter control with data-driven online adaptive optimization. Transp. Res. B 96, 26–45.
Lee, S., Wong, S.C., Varaiya, P., 2017. Group-based hierarchical adaptive traffic-signal control part I: Formulation. Transp. Res. B 105, 1–18.
Lei, T., Hou, Z., Ren, Y., 2019. Data-driven model free adaptive perimeter control for multi-region urban traffic networks with route choice. IEEE Trans. Intell. Transp. Syst..
Li, L., Huang, W., Lo, H.K., 2018. Adaptive coordinated traffic control for stochastic demand. Transp. Res. C 88, 31–51.
Li, Y., Yildirimoglu, M., Ramezani, M., 2021. Robust perimeter control with cordon queues and heterogeneous transfer flows. Transp. Res. C 126, 103043.
Lin, H., Antsaklis, P.J., 2009. Stability and stabilizability of switched linear systems: A survey of recent results. IEEE Trans. Automat. Control 54 (2), 308–322.
Ma, W., Zou, L., An, K., Gartner, N.H., Wang, M., 2018. A partition-enabled multi-mode band approach to arterial traffic signal optimization. IEEE Trans. Intell. Transp. Syst. 20 (1), 313–322.
Mariotte, G., Leclercq, L., Batista, S., Krug, J., Paipuri, M., 2020a. Calibration and validation of multi-reservoir MFD models: A case study in lyon. Transp. Res. B 136, 62–86.
Mariotte, G., Paipuri, M., Leclercq, L., 2020b. Dynamics of flow merging and diverging in MFD-based systems: Validation vs. Microsimulation. Front. Future Transp. 1, 3.
Mohajerpoor, R., Cai, C., 2020. Optimal traffic control for roads with mixed autonomous and human-driven vehicles.In: 2020 American Control Conference (ACC), pp. 4114–4119.
Mohajerpoor, R., Ramezani, M., 2019. Mixed flow of autonomous and human-driven vehicles: Analytical headway modeling and optimal lane management. Transp. Res. C 109, 194–210.
Mohajerpoor, R., Saberi, M., Ramezani, M., 2019. Analytical derivation of the optimal traffic signal timing: Minimizing delay variability and spillback probability for undersaturated intersections. Transp. Res. B 119, 45–68.
Mohajerpoor, R., Saberi, M., Vu, H.L., Garoni, T.M., Ramezani, M., 2020. H_∞ robust perimeter flow control in urban networks with partial information feedback. Transp. Res. B 137, 47–73.
Ni, W., Cassidy, M., 2019. City-wide traffic control: modeling impacts of cordon queues. Transp. Res. C.
Paipuri, M., Xu, Y., González, M.C., Leclercq, L., 2020. Estimating MFDs, trip lengths and path flow distributions in a multi-region setting using mobile phone data. Transp. Res. C 118, 102709.
Ramezani, M., Haddad, J., Geroliminis, N., 2015. Dynamics of heterogeneity in urban networks: Aggregated traffic modeling and hierarchical control. Transp. Res. B 74, 1–19.
Ramezani, M., Nourinejad, M., 2018. Dynamic modeling and control of taxi services in large-scale urban networks: A macroscopic approach. Transp. Res. C 94, 203–219.
Ren, Y., Hou, Z., Sirmatel, I.I., Geroliminis, N., 2020. Data driven model free adaptive iterative learning perimeter control for large-scale urban road networks. Transp. Res. C 115, 102618.
Saedi, R., Saeedmanesh, M., Zockaie, A., Saberi, M., Geroliminis, N., Mahmassani, H.S., 2020. Estimating network travel time reliability with network partitioning. Transp. Res. C 112, 46–61.
Saeedmanesh, M., Geroliminis, N., 2017. Dynamic clustering and propagation of congestion in heterogeneously congested urban traffic networks. Transp. Res. B 105.
Saffari, E., Yildirimoglu, M., Hickman, M., 2020. A methodology for identifying critical links and estimating macroscopic fundamental diagram in large-scale urban networks. Transp. Res. C 119, 102743.
Simoni, M., Pel, A., Waraich, R.A., Hoogendoorn, S., 2015. Marginal cost congestion pricing based on the network fundamental diagram. Transp. Res. C 56, 221–238.
Sirmatel, I.I., Geroliminis, N., 2021. Stabilization of city-scale road traffic networks via macroscopic fundamental diagram-based model predictive perimeter control. Control Eng. Pract. 109, 104750.
Sirmatel, I.I., Tsitsokas, D., Kouvelas, A., Geroliminis, N., 2021. Modeling, estimation, and control in large-scale urban road networks with remaining travel distance dynamics. Transp. Res. C 128, 103157.
Su, Z., Chow, A.H., Zheng, N., Huang, Y., Liang, E., Zhong, R., 2020. Neuro-dynamic programming for optimal control of macroscopic fundamental diagram systems. Transp. Res. C 116, 102628.
Wada, K., Usui, K., Takigawa, T., Kuwahara, M., 2018. An optimization modeling of coordinated traffic signal control based on the variational theory and its stochastic extension. Transp. Res. B 117, 907–925.
Yang, K., Menendez, M., Zheng, N., 2019. Heterogeneity aware urban traffic control in a connected vehicle environment: A joint framework for congestion pricing and perimeter control. Transp. Res. C 105, 439–455.
Yang, K., Zheng, N., Menendez, M., 2018. Multi-scale perimeter control approach in a connected-vehicle environment. Transp. Res. C 94, 32–49.
Yildirimoglu, M., Ramezani, M., 2020. Demand management with limited cooperation among travellers: A doubly dynamic approach. Transp. Res. B 132, 267–284.
Yildirimoglu, M., Ramezani, M., Geroliminis, N., 2015. Equilibrium analysis and route guidance in large-scale networks with MFD dynamics. Transp. Res. C 59, 404–420.
Yildirimoglu, M., Sirmatel, I.I., Geroliminis, N., 2018. Hierarchical control of heterogeneous large-scale urban road networks via path assignment and regional route guidance. Transp. Res. B 118, 106–123.
Zhang, L., Shi, P., 2009. Stability, l_2 -Gain and Asynchronous H_∞ control of discrete-time switched systems with average dwell time. IEEE Trans. Automat. Control 54 (9), 2192–2199.
Zheng, N., Geroliminis, N., 2020. Area-based equitable pricing strategies for multimodal urban networks with heterogeneous users. Transp. Res. A 136, 357–374.
Zhong, R., Chen, C., Huang, Y., Sumalee, A., Lam, W., Xu, D., 2018. Robust perimeter control for two urban regions with macroscopic fundamental diagrams: A control-Lyapunov function approach. Transp. Res. B 117, 687–707.